Separation and Purification Technology 335 (2024) 126079

Contents lists available at ScienceDirect

Separation and Purification Technology

journal homepage: www.elsevier.com/locate/seppur

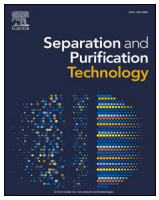

High-efficiency removal of Pb (II) and Cu (II) by amidoxime functionalized silica aerogels: Preparation, adsorption mechanisms and environmental impacts analysis

Yaoyao Zhang [a], Shikui Jia [a,*], Xinqiang Yuan [a], Liu Ding [a], Taotao Ai [a,*], Kangze Yuan [b], Wei Wang [c,*], Luca Magagnin [d], Zhenyi Jiang [e]

[a] School of Materials Science and Engineering, National and Local Joint Engineering Laboratory for Slag Comprehensive Utilization and Environmental Technology, Shaanxi University of Technology, Hanzhong, Shaanxi 723001, PR China
[b] College of Geological Engineering and Geomatics, Chang'an University, Xi'an, Shaanxi 710054, PR China
[c] School of Water and Environment, Chang'an University, Xi'an, Shaanxi 710054, PR China
[d] Department of Chemistry, Materials and Chemical Engineering "Giulio Natta", Politecnico di Milano, via Mancinelli 7, 20131 Milano, Italy
[e] Institute of Modern Physics, Northwest University, Xi'an, Shaanxi 710054, PR China

ARTICLE INFO

Editor: S. Deng

Keywords:
Heavy metal ions
Adsorption
Amidoxime
DFT
LCA

ABSTRACT

In this work, a novel adsorbent was evaluated for eliminating heavy metal ions from water. The cyano-functionalized silica aerogels (ANSA-X) were fabricated by functionalizing silica aerogel with 2-cyanoethyltriethoxysilane, and then further by the reaction with hydroxylamine hydrochloride to obtain amidoxime-functionalized silica aerogels (AOSA-X) with a large specific surface area. The FTIR and NMR analysis indicated that cyano was successfully transformed into amidoxime groups. Adsorption experiments showed the adsorption performed well with the Langmuir isotherm, and AOSA3 exhibited the optimum adsorption property with 598.05 mg/g for Pb (II) and 534.10 mg/g for Cu (II). The thermodynamic results indicated that spontaneous endothermic process was the nature of the adsorption. The adsorption rate of AOSA3 was above 86% after five successive adsorption–desorption cycles. XPS analysis and DFT calculations demonstrated that the N and O atoms participated in the chelating adsorption of Pb (II) and Cu (II), and the N atom on the amidoxime groups played a dominant role. Life Cycle Analysis (LCA) evaluated the environmental effect of the preparation of 1 kg AOSA3 adsorbent, identified the environmental factors with high environmental impact, proposed alternative solutions, proved the feasibility of preparing a novel high-efficiency amidoxime-based adsorbent, and provided a guideline for the sustainable mass production of AOSA3 adsorbent. In conclusion, AOSA3 demonstrated to have promising application perspectives in heavy metal effluent treatment.

1. Introduction

Great advances in science and technology have led to industrial development that has made life easier for human beings. However, the development of global industry is often associated with environmental pollution, and the emission of industrial wastewater has led to rising heavy metal concentrations in water, causing unreversible impacts on nature [1]. Heavy metal pollution possesses permanent, non-degradable, and bio-accumulative properties, and will eventually cause great harm to human beings through the amplification of the food chain layer by layer [2,3]. Lead is one of the most hazardous metal contaminants and can lead to brain damage, high blood pressure, anorexia, reproductive organ damage, cause kidney failure and Fanconi-like syndrome [4]. Copper is probably deemed essential, but a wide range of health complications may arise with increased intake and high levels of exposure, which may trigger stomach disorders, central nervous system irritation, kidney function decline, and lead to Alzheimer's disease [5]. Therefore, heavy metal pollution has become a serious issue for environmental treatment in the current global environment.

Currently, various remediation methods and technologies, including chemical precipitation [6], biological methods [7], membrane separation technology [8], ion exchange [9], electrochemical methods [10] and adsorption methods [11]. Adsorption is widely regarded as an efficient and appealing method owing to its high adsorption efficiency,

* Corresponding authors.
E-mail addresses: shikuijia@snut.edu.cn (S. Jia), aitaotao0116@126.com (T. Ai), wwchem@126.com (W. Wang).

https://doi.org/10.1016/j.seppur.2023.126079
Received 7 October 2023; Received in revised form 7 November 2023; Accepted 21 November 2023
Available online 21 December 2023

cost-effective and environmentally friendly nature [12]. Many researchers have explored the removal of Pb (II) and Cu (II) by a variety of different adsorbents including chitin [13], graphene [14], attapulgite [15], mesoporous silica [16], chitosan [17], kaolinite [18], biochar [19], geopolymer [20], clay [21], and zeolite [22]. However, these adsorbents have the disadvantages of low adsorption efficiency and difficult regeneration [12]. Therefore, it is urgent to develop and to exploit high-efficiency and recyclable adsorbents.

With high specific surface area, high thermodynamic stability, high porosity and environmental friendliness, silica aerogels are expected to overcome the disadvantages by using them as carriers [23]. The amidoxime group possesses both an amino group and an oximido group, which can be expressed as –C(NOH)NH_2, having excellent metal ion chelating properties [24]. The early use of amidoxime chelate materials was mainly for seawater uranium extraction, due to the high affinity of amidoxime (AO) for UO_2^{2+}, it was widely considered as one of the most promising binding sites for UO_2^{2+} [25]. Due to the extremely strong chelating and ligating ability of amidoxime groups, amidoxime chelating materials are becoming more and more attractive for the removal of heavy metal ions [26]. Cross-linked amidoxime polyacrylonitrile microspheres (H-CAN) were prepared by grafting N'-methylene bis(acrylamide) into polyacrylonitrile followed by treatment with hydroxylamine hydrochloride. The maximum adsorption amounts of H-CAN was 113.13 mg/g for Pb (II) and 140.33 mg/g for Cu (II) [27]. Zhao et al. obtained amidoxime-functionalized polypropylene fiber (AO-PP) by graft copolymerization of acrylonitrile (AN) on polypropylene (PP) fiber and transformed into amidoxime (AO) groups via a reaction of the fiber with hydroxylamine hydrochloride solution. The maximum adsorption by AO-PP was 45.64 mg/g for Pb (II) and 47.23 mg/g for Cu (II) [28]. Firstly, vinyl modified seafoam was obtained by functionalizing seafoam with coupling agent vinyl triethoxysilane. Acrylonitrile monomers were grafted on vinyl-modified seafoam using gamma rays, and then reacted with hydroxylamine hydrochloride to prepare amidoxime chelated adsorbent (AO-RGS). The samples irradiated at 5 kGy showed the optimum adsorption of Cu (II) with a maximum adsorption of 278 mg/g [29]. Xie et al. synthesized fibrous cyano-modified mesoporous SiO_2 microspheres using 2-cyanoethyltriethoxysilane as raw material, and then transformed the cyano into amidoxime groups to obtain amidoxime-functionalized SiO_2 microspheres with a maximum adsorption towards Pb (II) of 284 mg/g, which is a prospective heavy metal ion adsorbent [30]. Therefore, it is valuable to exploit the feasibility of high-efficiency heavy metal ion adsorbents with high adsorption capacity, stable structure, and easy recycling via the incorporation of excellent chelating performance of amidoxime groups and the specific properties of silica aerogels.

There is a shortage of profound understanding of the heavy metal ions adsorption mechanism by adsorbents. Density Functional Theory (DFT) calculations have been widely used as a powerful tool in physics, chemistry, and materials, which can provide a profound understanding of the adsorption mechanism of heavy metal ions at the atomic level [31]. Meanwhile, researchers have paid little consideration to the environmental implications of the aerogel fabrication process. Life Cycle Analysis (LCA) is used to quantify products, services, resource consumption, as well as related environmental and health effects based on environmental and health impacts [32]. LCA analysis gives a clear overview of the impact on the environment in the early stages of product preparation, and it is useful to mitigate the impact on the environment by modifying or changing the factors that have a negative impact on the environment [33,34].

In view of the above-mentioned concerns, cyano-functionalized silica aerogels (ANSA-X) were first obtained by using 2-cyanoethyltriethoxysilane (CTES) and ethyl orthosilicate (TEOS) under atmospheric pressure drying (APD) conditions. Then, by reaction with hydroxylamine hydrochloride solution, the amidoxime (AO) group was introduced into the ANSA-X aerogels, which resulted in a high chelating ability of the AOSA-X for heavy metal ions. The influence of different levels of cyanosilane coupling agents on the morphology, microstructure and specific surface area of the generated AOSA-X samples were investigated. The adsorption properties of AOSA-X on Pb (II) and Cu (II) were studied, and the adsorption mechanism was interpreted by combining XPS analysis, ^{1}H NMR and DFT theoretical calculations. Finally, the environmental effects of the amidoxime functionalized silica aerogels production process was assessed by LCA method. The findings of this work will be useful for the prospective design of heavy metal adsorbent strategies with excellent properties, rapidity and environmental friendliness for large-scale applications.

2. Experimental methods

2.1. Materials

2-Cyanoethyltriethoxysilane (CTES) was purchased from Shanghai Aladdin Base Ltd. Ethyl orthosilicate (TEOS), anhydrous ethanol (ETOH), n-Hexane, hydrochloric acid, sodium hydroxide, ammonia, hydroxylamine hydrochloride ($NH_2OH{\cdot}HCl$), sodium carbonate, copper (II) chloride, nickel(II) chloride, cadmium(II) chloride, zinc(II) chloride, manganese(II) chloride, and lead(II) chloride were obtained from Sinopharm Chemical Reagent Co.

2.2. Preparation of cyano-functionalized silica aerogels (ANSA-X)

The first step involved dissolving 10 mL of TEOS in anhydrous ethanol, followed by pH adjustment to 3 using 0.1 M HCl (wherein all water was substituted with 0.1 M HCl). The mixture was then agitated and heated at 60 °C for a duration of 2 h. Then, different levels of CTES were introduced and the reflux reaction was kept at 60 °C for 2 h. Afterward, the pH was adapted to 7.0 by adding 1 M ammonia, agitated violently for about 5 min, and moved to the mold. After the wet gel was formed, the gel was aged in ethanol over 24 h and then exchanged with ethanol 6 times (within 48 h) and with n-Hexane 4 times (within 48 h) in a water buffer at 40 °C for elimination of excess moisture and retained organic compounds. Finally, the wet gels were dried under 40 °C atmospheric pressure for 48 h resulting in cyano-functionalized silica aerogels (ANSA-X). The TEOS/ETOH/H_2O molar ratio was 1:10:16. The corresponding synthetic samples were named ANSA1, ANSA2, ANSA3 and ANSA4 based on the CTES/TEOS molar ratios of 0.1, 0.2, 0.3 and 0.4, respectively.

2.3. Preparation of amidoxime functionalized silica aerogels (AOSA-X)

Firstly, 1.3898 g of hydroxylamine hydrochloride was taken into 25 mL of deionized water and agitated until fully dissolved. And 1.10 g of sodium carbonate was added and heated to 70 ℃ with stirring. Then, 1.0 g of sieved ANSA-X aerogels were added and stirred magnetically at 70 ℃ for 3 h. After centrifugal filtration and washing with deionized water, the AOSA-X samples were obtained by drying at 60 °C overnight. According to the different CTES contents mentioned above, the corresponding samples were named AOSA1, AOSA2, AOSA3, and AOSA4, respectively, and the synthesis process was shown in Fig. 1. Among them, AOSA3 was singled out for the subsequent adsorption mechanism study and LCA evaluation, as it demonstrated the optimum adsorption property. The monomeric amidoxime sample (AO) was obtained by reacting 2-cyanoethyltriethoxysilane with hydroxylamine hydrochloride by exactly the same experimental method except for the absence of TEOS. After the reaction of monomer AO with Pb (II) and Cu (II) solutions, AO-Pb (II) and AO-Cu (II) were obtained, respectively.

2.4. Characterization

The surface morphology of the functionalized silica aerogels was determined using scanning electron microscope (Hitachi S-4800, Japan). The material phase composition was ascertained by X-ray

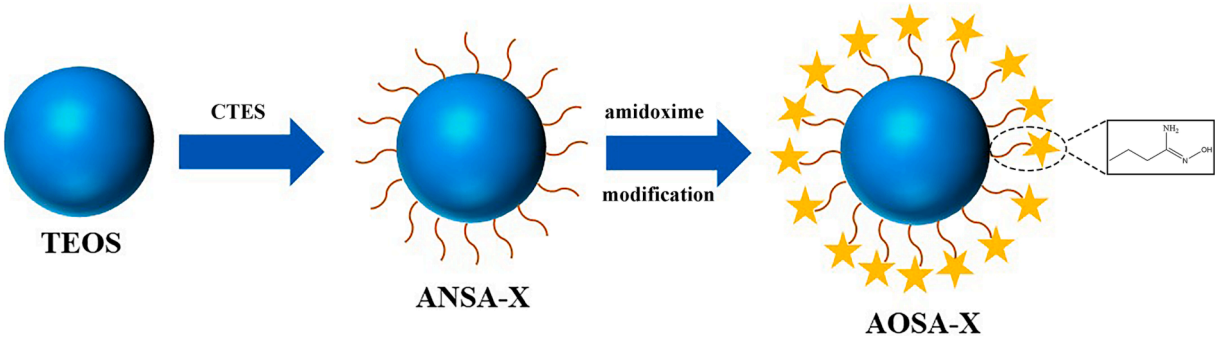

Fig. 1. Schematic synthesis of amidoxime functionalized silica aerogels.

diffraction (XRD) using a D8 ADVANCE diffractometer. The functional group characteristics of the functionalized silica aerogels were analyzed using the ATR method with a fourier infrared spectrometer (Nicolet 5700 spectrometer). Isothermal N_2 adsorption–desorption of functionalized aerogels were measured by the NOVA 2200 specific surface area and pore size analyzer. Element content measurement of functionalized aerogels using the Elementar Vario EL Cube elemental analyzer. ^{1}H NMR spectra and ^{13}C NMR spectra were recorded using a JAPAN-JEOL 400 MHz spectrometer (with $CDCl_3$ as solvent) to characterize CTES, AO, AO-Pb (II) and AO-Cu (II). Thermal stability of functionalized aerogel samples were characterized by Setaram Labsys Evo thermogravimetric differential thermal instrument. X-ray photoelectron spectroscopy (XPS) was obtained by ESCALAB 250 (USA) instrument for analyzing the chemical composition and elemental valence of functionalized silica aerogel samples before and after adsorption. The concentration of heavy metal ions was detected by a WFX-120 Atomic Absorption Spectrophotometer (AAS) from Beijing Ruili Analytical Instruments Co.

2.5. Heavy metal ion adsorption experiments

A series of centrifuge tubes containing different levels of adsorbents were tested for adsorption properties with 20 mL of 50 mg/L of heavy metal solutions. The impact of pH on the removal of Pb (II) and Cu (II) by AOSA-X was examined with the variation of initial pH between 1.0 and 6.0. Adsorption kinetics experiments were undertaken with 20 mg of adsorbent and 20 mL of heavy metal ion solution at different time intervals from 0 to 180 min. Isothermal adsorption tests were conducted over an initial concentration range of 50–1000 mg/L. Adsorption thermodynamics experiments were conducted at varying temperatures ranging from 293 K to 318 K. Following every adsorption, the reusability was assessed by adding the saturated sorbent to HCl solution (0.1 M) and stirring over 180 min for desorption. Three replications of each experiment were undertaken and the average values were reported. The removal rate (φ, %) and adsorption capacity (q, mg/g) were measured by Eqs. (1) and (2):

$$\varphi = \frac{c_0 - c}{c_0} \times 100\% \tag{1}$$

$$q = \frac{(c_0 - c) \times v}{w} \tag{2}$$

Where the initial and time t concentration of heavy metal ions are denoted as c_0 (mg/L) and c (mg/L), respectively. The adsorbent dosage is indicated by w (g), while the solution volume is represented by v (L).

Further details on the isotherm, kinetic and thermodynamic modeling can be found in the Supporting Information (S1).

2.6. DFT calculation

The DFT calculations were carried out using Gaussian 09 software [35]. The simulations were performed in the base state using B3LYP exchange-related hybrid functionals [36]. In this case, the heavy metals Pb and Cu were described by the LanL2DZ basis set, while 6–31 g(d) was employed for other atoms during geometry optimization and frequency calculations. For single point energy calculations, a larger combination of basis sets was used, with the LanL2DZ basis set applied to Pb and Cu, and 6–311 g(d, p) utilized for other atoms [37]. The adsorption energies (E_{ads}) were computed from Eq. (3) [38]:

$$E_{ads} = E_{total} - (E_{adsorbent} + E_{metal}) \tag{3}$$

Where the energy of AOSA3-Pb or AOSA3-Cu is expressed as E_{total}, the energy of AOSA3 is replaced by $E_{adsorbent}$, and the energy of Pb or Cu atom is expressed as E_{metal}.

2.7. LCA analysis

2.7.1. Objective and scope definition

Life Cycle Analysis (LCA) is a validated and applicable methodology for estimating the environmental footprint of a product throughout its life cycle. The LCA approach was applied to assess the environmental effect of the preparation of 1 kg of AOSA3. The eFootprint software package was adopted to calculate the environmental impact, according to the ISO 14044 guidelines [39]. Following an assessment of the environmental contribution from each raw material involved in the production of adsorbents, we identified environmental hotspots and proposed substitute environmentally efficient production solutions in order to alleviate the negative impacts on sustainable development. This can possibly facilitate the widespread usage of adsorbents in the adsorbent market.

The system boundaries for this work include the generation and transportation of the original materials that constitute the adsorbent and its synthesis (Fig. S1). The transport distances of the original materials were determined using the average distance of goods transported as a baseline measure (181 km). There is no need for disposal at the end-of-life stage because of the non-impact on the environment in the usage stage. The utilization and end-of-life stages were not considered in this work.

2.7.2. Life cycle inventory analysis

A critical function of inventory analysis in the overall evaluation is to uncover all the outputs and inputs of the whole production process. According to the experiments gathered in our laboratory, we conducted calculations with eFootprint using the Ecoinvent database v.3.1, and accessed everything available from the Life Cycle Inventory (LCI) using the CLCD. This study supposed that the global average power mix was used as the production supply. The life cycle inventory of adsorbents can be found in Table 1. The assessment methodology is associated with the selection of the environmental impact category [40], and Life Cycle Impact Assessment methodology was in Supporting Information (S2).

Table 1
Life cycle inventory of the preparation of 1 kg AOSA3.

	Mass	Unit
Raw material input		
TEOS	0.62	kg
Ethanol	20	kg
n-Hexane	18.29	kg
Water	2.96	kg
HCl	10	g
NH_3	7.85	g
$NH_2OH{\cdot}HCl$	91.73	g
Na_2CO_3	72.6	g
CTES	191.93	g
Energy input		
Electricity	8	kWh
Transportation	181	km
Output		
AOSA3	1	kg

3. Results and discussion

3.1. Characterization

Fig. 2 showed the SEM images of the ANSA-X and AOSA-X samples. The surface morphology of the ANSA-X samples changed considerably with the change of the CTES content. When n(CTES): n(TEOS) = 0.1, the ANSA1 sample was very dense and shrunken (Fig. 2a). As the CTES content increased, the structure of the silica aerogel samples became increasingly sparse and the sample particles became larger. The AOSA-X samples agglomeration became more compact, but still maintained a porous structure. The morphology of the AOSA-X samples exhibited a rich pore distribution, facilitating the migration and diffusion of metal ions to the AOSA-X surface. According to Table S1, the nitrogen content of the materials increased as the CTES content increased, with the elemental N content of ANSA1, ANSA2, ANSA3 and ANSA4 being 1.37, 2.26, 2.90 and 3.43 mmol/g, respectively. And the elemental N content of AOSA1, AOSA2, AOSA3 and AOSA4 were 1.34, 2.46, 3.38 and 4.08 mmol/g, respectively.

The FTIR spectra were investigated to identify the chemical composition of the ANSA-X and AOSA-X in Fig. 3. The peaks at 458, 775 and 1112 cm^{-1} were divided into Si-O-Si bending vibrational, symmetric and asymmetric vibrational peaks [41]. The band at 3452 cm^{-1} was an O–H vibrational peak. The vibration related to C–H symmetric and asymmetric vibrational peaks appeared at 2921 and 2813 cm^{-1} [42]. Moreover, a peak at 2260 cm^{-1} was noted in the ANSA-X sample, corresponding to C≡N stretching vibration [43]. The intensity of the cyano peak gradually became larger as the CTES content increased. In the AOSA-X samples, the cyano peak almost disappeared, proving that

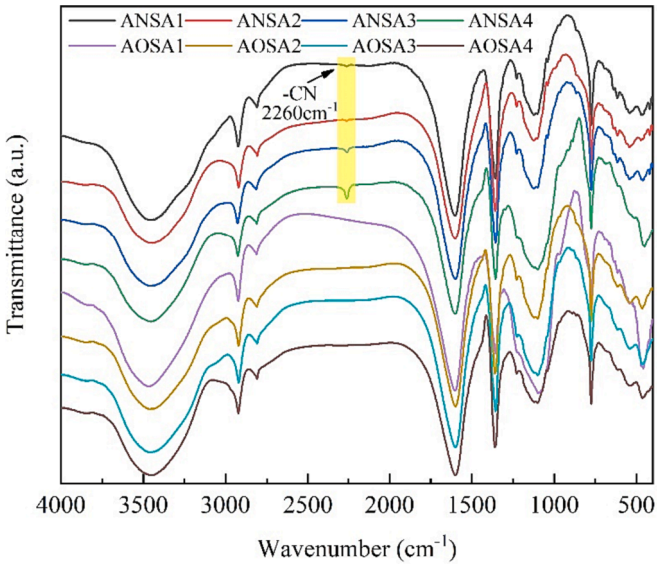

Fig. 3. The FTIR spectra of samples.

the cyano group has been successfully reacted to form the amidoxime groups, and the generated C=N and C–N bonds overlapped with O–H (1602 cm^{-1}) and C–H (1381 cm^{-1}), respectively [44]. The XRD spectra of ANSA3 and AOSA3 were presented in Fig. S2. Both ANSA3 and AOSA3 samples exhibited broad diffraction peaks around 22°, which were assigned as amorphous silica structure [45]. The AOSA-X samples showed three sharp diffraction peaks at 31.7°, 45.4° and 56.5°, which were ascribed to the characteristic peaks of the amidoxime groups [29], indicating the successful synthesis of amidoxime functionalized silica aerogels.

The ^1H NMR and ^{13}C NMR spectra of CTES and AO were presented in Fig. S3. In Fig. S3a, the peak that appeared at 2.34 ppm was ascribed to the $–CH_2$ linked to –CN. In the AO sample, the disappearance of the peak at 2.34 ppm was accompanied by the appearance of an amino peak (5.17 ppm) and a hydroxyl peak (9.03 ppm), which indicated that the cyano group had been converted to the amidoxime group [46]. In Fig. S3b, the peak at 120.95 ppm was attributed to –CN of CTES, and the presence of the amidoxime carbon [$-C(NH_2)NOH$] at 160.08 ppm on AO demonstrated the successful reaction to generate amidoxime group [47,48]. Fig. 4 showed the N_2 adsorption–desorption isotherm plots for the AOSA-X samples. All samples displayed typical type IV isotherms based on IUPAC classification, indicating that the AOSA-X samples had a mesoporous structure. The hysteresis can be clearly seen in the region where P/P_0 is 0.4–0.9, and it may belong to the H1 type hysteresis loop,

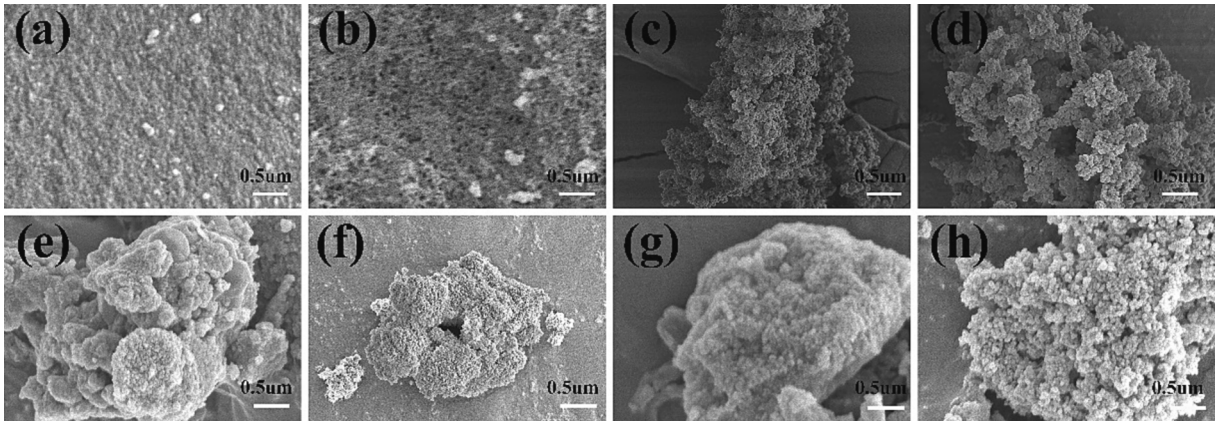

Fig. 2. The SEM analysis of samples: (a) ANSA1, (b) ANSA2, (c) ANSA3, (d) ANSA4, (e) AOSA1, (f) AOSA2, (g) AOSA3, (h) AOSA4.

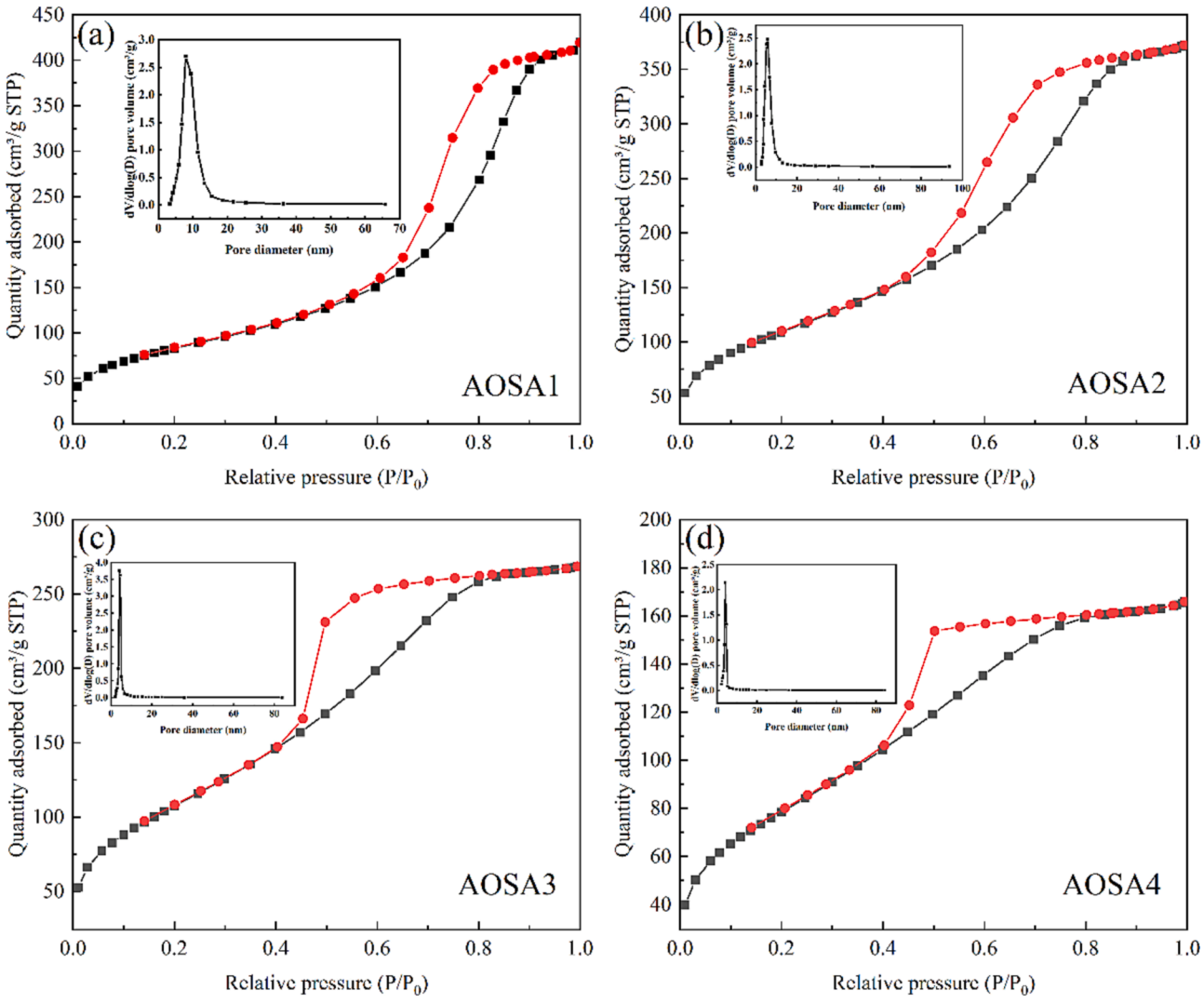

Fig. 4. N_2 adsorption–desorption isotherms and pore size distribution curves.

implying that the AOSA-X samples had a narrow pore size distribution. Besides, the pore size distribution curve further demonstrated that AOSA-X had a narrow pore size distribution. From Table S2, it was observed that the specific surface area of the AOSA-X samples increased and then decreased as the CTES content increased, with the AOSA2 sample possessing the largest specific surface area, followed by AOSA3.

As observed in Fig. S4, the mass loss below 120 °C was owing to the weight loss of physically adsorbed water from the test samples. There are two weight loss stages for the ANSA-X samples at 120–550 °C and 550–660 °C, associated with the decomposition of organic components, including the decomposition of cyano groups [49]. Between 120 and 660 °C, the mass losses of ANSA1, ANSA2, ANSA3 and ANSA4 were 10.13%, 12.62%, 14.98% and 15.70%, respectively. And the mass losses of the AOSA1, AOSA2, AOSA3 and AOSA4 samples were 12.98%, 14.99%, 17.41% and 18.55% at 120–600 °C, respectively, relating to the thermal decomposition of the amidoxime moiety [50]. The total thermogravimetric losses of the AOSA1, AOSA2, AOSA3 and AOSA4 samples were 27.67%, 29.68%, 31.81% and 32.4%, respectively. These phenomena are indicative of the lower thermal stability of the AOSA-X samples in comparison to the ANSA-X samples.

3.2. Adsorption performance

3.2.1. Effect of adsorbent dosage

ANSA-X samples were obtained by using varying CTES and TEOS molar ratios in the sol–gel synthesis process, and AOSA-X samples were obtained after the amidoxime modification. As depicted in Fig. 5, AOSA3 had the optimum removal of Pb (II) and Cu (II) at a CTES/TEOS molar ratio of 0.3. It may be attributed that as the CTES/TEOS molar ratio increased, the specific surface area of the aerogel samples increased and then decreased, the aerogel samples particles became larger and less dense, and ANSA-X samples with more functional groups can be obtained, providing more reactive functional groups for further amidoxime modification. However, when the molar ratio of CTES/TEOS increased to 0.4 (AOSA4), the metal ions were unable to access these functional groups due to the remarkable drop in specific surface area leading to severe particle aggregation. Therefore, AOSA3 was elected for the follow-up study, and the adsorbent dosage of 0.02 g was selected as having the optimum adsorption performance and economy for the adsorption test.

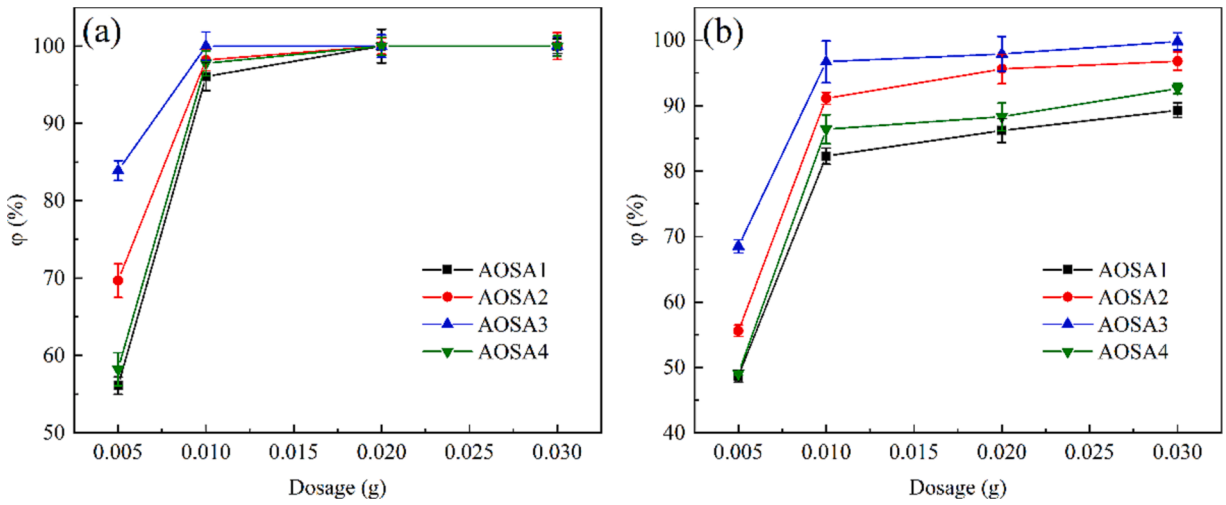

Fig. 5. Influence of various CTES/TEOS molar ratios on the adsorption of Pb (II) (a) and Cu (II) (b) (conditions: V = 20 mL, c_0 = 50 mg/L, T = 298 K, pH = 5).

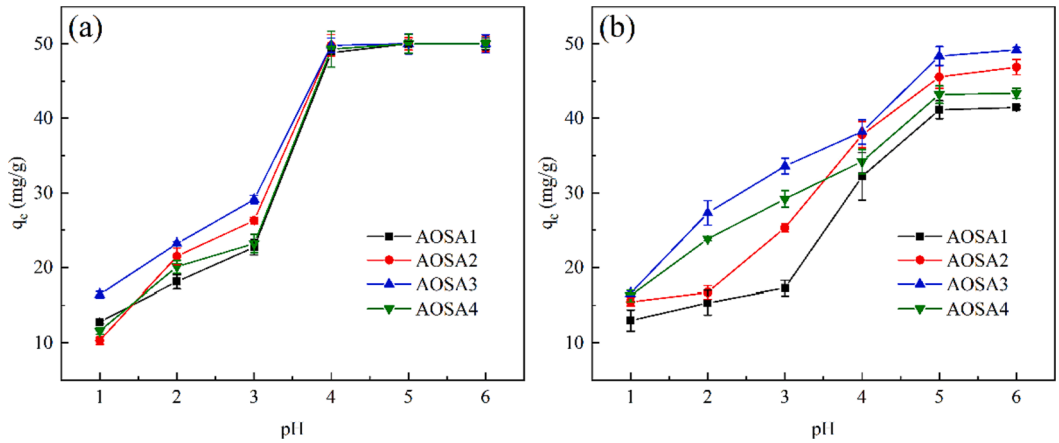

Fig. 6. Impact of pH value on the adsorption of Pb (II) (a) and Cu (II) (b) (conditions: V = 20 mL, c_0 = 50 mg/L, T = 298 K, adsorbent dosage: 20 mg).

3.2.2. *Effect of pH*

The impact of pH on metal ions adsorption by AOSA-X was displayed in Fig. 6. When pH < 3, the H^+ concentration in solution was high, causing the protonation of the amidoxime groups on AOSA-X. The protonated AOSA-X samples generated electrostatic repulsion towards heavy metal cations, thus reducing the adsorption of the metal ions. The adsorption of AOSA-X on Pb (II) and Cu (II) increased rapidly from pH 3 to 5 and attained a maximum value in pH 5. As can be seen from Fig. S5, the point of zero charge (pH_{pzc}) of AOSA3 was approximately 4.1. At pH values <4.1, the surface of AOSA3 was positively charged, restricting the adsorption of metal cations. At pH value >4.1, the surface of AOSA3 gradually became negatively charged and the repulsive effect gradually diminished [51]. The pH equal to 5 was chosen for further tests.

3.2.3. *Adsorption kinetics*

Fig. S6 exhibited the effect of reaction time on the removal of metal ions by AOSA-X. It can be observed that with increasing adsorption time, AOSA-X exhibited fast adsorption towards Pb (II), reaching the equilibrium within 60 min, and the adsorption towards Cu (II) was reached equilibrium at about 120 min. Apparently, AOSA-X reached equilibrium faster for Pb (II) adsorption than Cu (II) adsorption.

Adsorption processes were investigated using the pseudo-first-order, pseudo-second-order, intraparticle diffusion and Elovich kinetic models. The nonlinear adsorption kinetic curves and results were displayed in Figs. 7, 8 and Table 2. Both the pseudo-first-order ($R^2 > 0.98$) model and pseudo-second-order ($R^2 > 0.99$) model conformed well to the experimental data, with the pseudo-first-order model presumed to be diffusion-dominated and the pseudo-second-order model assumed to be chemisorption-dominated, suggesting that both diffusion and chemisorption participated in the adsorption process [52,53]. The Elovich model also fitted the experimental data better, suggesting that the adsorption was controlled by chemical interactions [27]. Moreover, the intraparticle diffusion model presented three linear segments, suggesting that the adsorption process involved multi-steps. There was an external diffusion in the first stage, where heavy metal ions diffused rapidly to the exterior surface of AOSA-X from the solution. There was an intra-particle diffusion in the second stage, where the diffusion rates of metal ions were lower than the first stage. At the third stage, there was a progressive decrease and saturation of the reactive sites, and the adsorption achieved equilibrium. Therefore, the intraparticle diffusion modeling results indicated that the adsorption involved several kinetic stages [54]. Overall, the results indicated that the adsorption of Pb (II) and Cu (II) on AOSA-X occurred through physisorption and chemisorption mechanisms.

3.2.4. *Adsorption isotherm*

The effect of different initial concentrations on metal ions adsorption by AOSA-X was investigated (Fig. S7). The adsorption of metal ions by AOSA-X increased with the growth of the initial concentration, and as the initial concentration raised to 800 mg/L, the adsorption was almost ceased to increase, indicating that the adsorption had reached saturation. The maximum adsorption of Pb (II) by AOSA-X was greater than

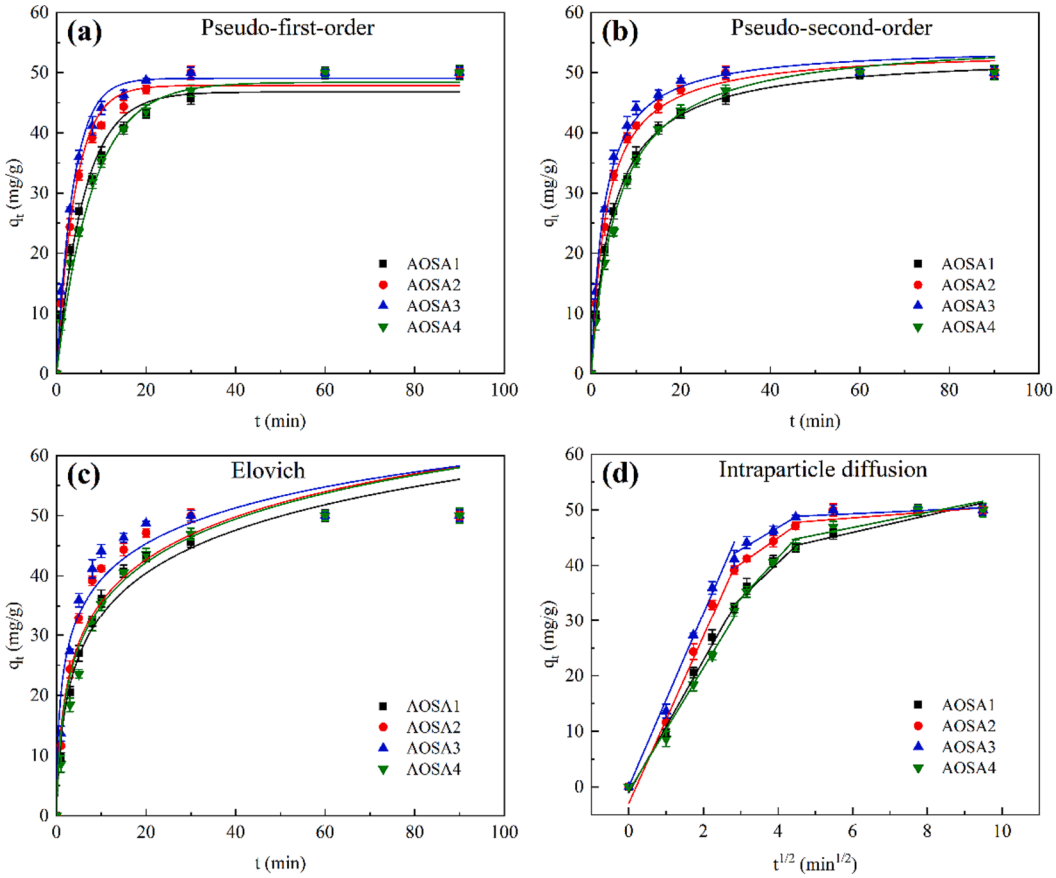

Fig. 7. Adsorption kinetics of Pb (II) on AOSA-X (conditions: V = 20 mL, c_0 = 50 mg/L, T = 298 K, adsorbent dosage: 20 mg).

that of Cu (II), and AOSA3 showed the optimum adsorption property for heavy metal ions.

The adsorption isotherms were analyzed by Langmuir, Freundlich, Temkin and Dubinin-Radushkevich (D-R) models, and the fitted curves and its associated parameters were shown in Figs. 9, 10 and Table 3. The Langmuir model exhibited high R^2 values ranging from 0.9397 to 0.9942, demonstrating that monomolecular layer adsorption took place on the AOSA-X surface. The maximum adsorption (q_m) of Pb (II) by AOSA1, AOSA2, AOSA3 and AOSA4 were 453.53, 505.14, 598.05 and 511.75 mg/g, respectively, and the corresponding experimental measured values (q_e) were 442.40, 484.60, 578.21 and 473.67 mg/g, respectively. Similarly, the maximum calculated adsorption capacities (q_m) of AOSA1, AOSA2, AOSA3 and AOSA4 for Cu (II) were 417.08, 480.40, 534.10 and 417.51 mg/g, respectively, and the experimental measured values (q_e) were 364.21, 438.11, 486.73 and 382.08 mg/g, respectively. The Langmuir constant (K_L) for Pb (II) adsorption by AOSA-X was greater than Cu (II), suggesting that amidoxime possessed a higher affinity for Pb (II) [55]. In addition, the Freundlich model was also associated well with K_F [Cu (II)] < K_F [Pb (II)] (R^2, 0.90–0.97), indicating that the affinity of AOSA-X for Pb (II) was higher than Cu (II) [56]. And the n values were higher than 0 and smaller than 1, implying favorable adsorption. Furthermore, the Temkin model also fitted the adsorption data well (R^2, 0.81–0.98), suggesting that the adsorption was likely impacted by adsorbate and adsorbent interactions [57]. Besides, the R^2 values calculated from the D-R model ranged from 0.8472 to 0.9426, indicating that the adsorption of Pb (II) and Cu (II) by AOSA-X conformed to the pore-filling mechanism (E < 8 kJ/mol) [58,59]. Thus, the Langmuir model was more suitable for describing the adsorption of Pb (II) and Cu (II) on the AOSA-X material than the other models, with the highest value of Langmuir isotherm correlation coefficients (R^2), indicating that the adsorption involved both chemisorption and pore-filling mechanism and was mainly influenced by chemisorption.

The comparison of the adsorption capacity of Pb (II) and Cu (II) between other amidoxime-based adsorbents reported in the literature and AOSA-X was shown in Table 4. Combined with XPS analysis, NMR analysis, DFT calculations, and in conjunction with the adsorption results, the high adsorption performance of AOSA3 for Pb (II) and Cu (II) was mainly dependent on two aspects, one was the complex adsorption of heavy metal ions by the reactive functional group of amidoxime groups on the surface of the adsorbent, and the other was attributed to the large specific surface area of AOSA3 and the physical adsorption by the filling of the pores. In general, AOSA-X possessed high adsorption capacity towards Pb (II) and Cu (II) making it a prospective heavy metal adsorbent.

3.2.5. *Adsorption thermodynamics*

The influence of various temperatures upon AOSA-X for metal ions adsorption was demonstrated in Fig. S8. Increasing the temperature facilitated the adsorption reaction and increased Pb (II) and Cu (II) adsorption by AOSA-X, indicating the adsorption was an endothermic process. The influence of temperature towards Cu (II) adsorption by AOSA-X was more pronounced. The relationship between lnk_c and $1/T$ was shown in Fig. 11, which gave the intercepts and slopes used to calculate the ΔS^0 and ΔH^0 parameters, with corresponding parameters presented in Table 5.

As observed in Table 5, the negative values of ΔG^0 for metal ions adsorption by AOSA-X suggested that the adsorption was viable and thermodynamically spontaneous. The ΔG^0 values changed between −20 and 0 kJ/mol, implying that the adsorption process concerned physical adsorption in the thermodynamic range studied [63]. ΔH^0 values were positive, demonstrating that the adsorption was endothermic and the adsorption of Pb (II) and Cu (II) by AOSA-X increased

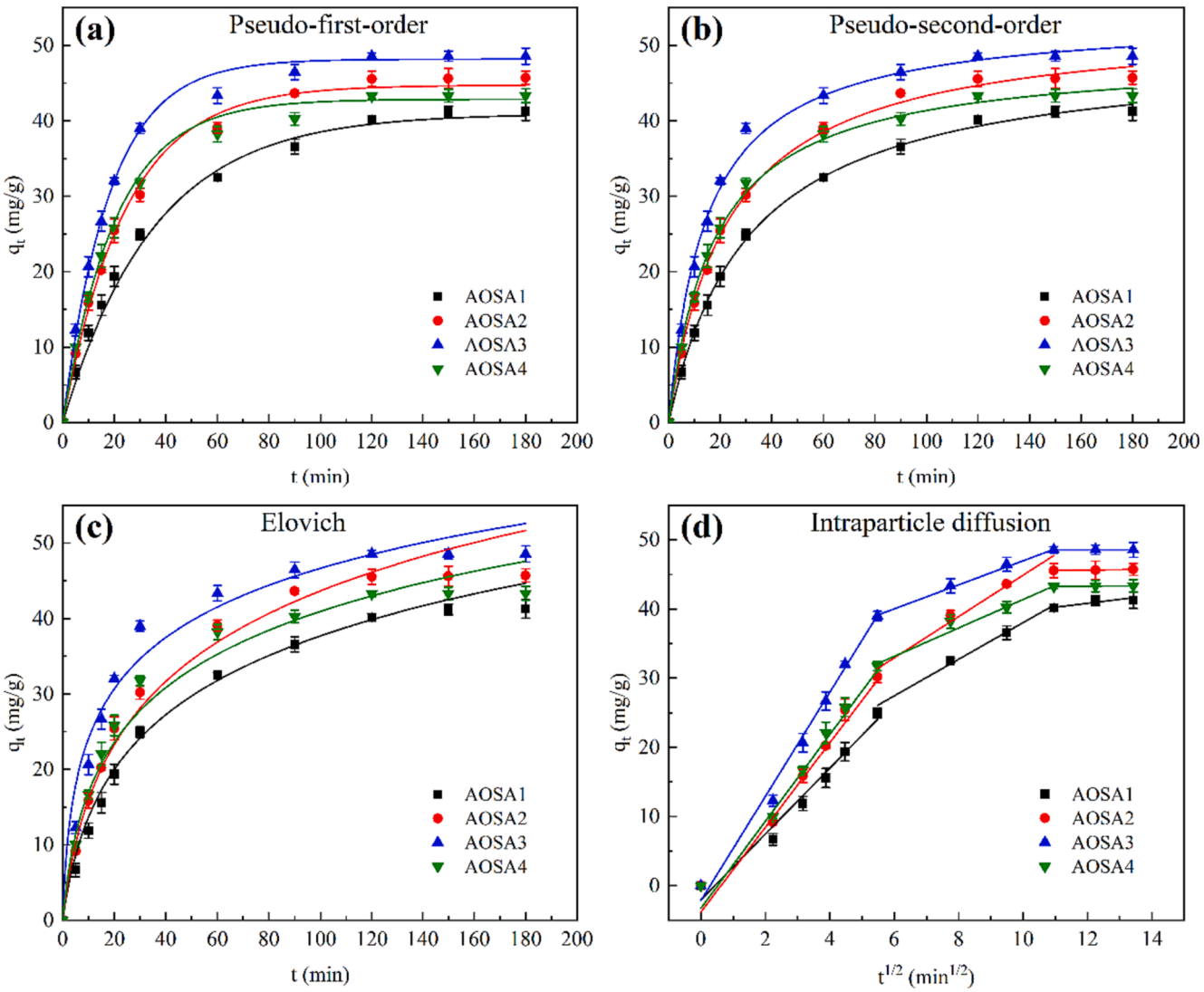

Fig. 8. Adsorption kinetics of Cu (II) on AOSA-X (conditions: V = 20 mL, c_0 = 50 mg/L, T = 298 K, adsorbent dosage: 20 mg).

Table 2
Adsorption kinetic parameters for Pb (II) and Cu (II) onto AOSA-X.

Kinetic models	Parameters	Pb (II)				Cu (II)			
		AOSA1	AOSA2	AOSA3	AOSA4	AOSA1	AOSA2	AOSA3	AOSA4
Pseudo-first-order	k_1 (min^{-1})	0.1631	0.2415	0.2690	0.1251	0.0282	0.0409	0.0546	0.0483
	q_e (mg/g)	46.78	47.86	49.04	48.38	40.93	44.72	48.16	42.85
	R^2	0.9825	0.9909	0.9959	0.9917	0.9911	0.9967	0.9963	0.9961
Pseudo-second-order	k_2 (g/(mg·min)	0.0039	0.0055	0.0065	0.0031	0.0006	0.0008	0.0013	0.0011
	q_e (mg/g)	53.22	53.93	54.36	55.89	49.45	53.18	53.87	48.75
	R^2	0.9991	0.9967	0.9918	0.9945	0.9988	0.9976	0.9947	0.9977
Elovich	α (mg/(mg·min)	24.18	31.07	82.59	27.89	2.51	2.97	9.84	3.87
	β (mg/g)	0.0952	0.0962	0.1160	0.0943	0.0812	0.0708	0.0982	0.0865
	R^2	0.9753	0.9361	0.9231	0.9467	0.9908	0.9876	0.9645	0.9855
Intraparticle diffusion	k_{p1} (mg/(g·$min^{1/2}$))	11.92	15.07	15.61	11.09	4.75	6.11	7.52	6.27
	R^2	0.9922	0.9892	0.9917	0.9935	0.9764	0.9797	0.9895	0.9856
	k_{p2} (mg/(g·$min^{1/2}$))	6.41	4.69	3.99	7.38	2.64	2.98	1.73	2.05
	R^2	0.9735	0.9963	0.9814	0.9743	0.9853	0.9619	0.9979	0.9908
	k_{p3} (mg/(g·$min^{1/2}$))	1.5275	0.5231	0.3101	1.3539	0.5771	0.0652	0.0052	0.0241
	R^2	0.9096	0.6829	0.7559	0.8415	0.8688	0.9936	0.8550	0.8793

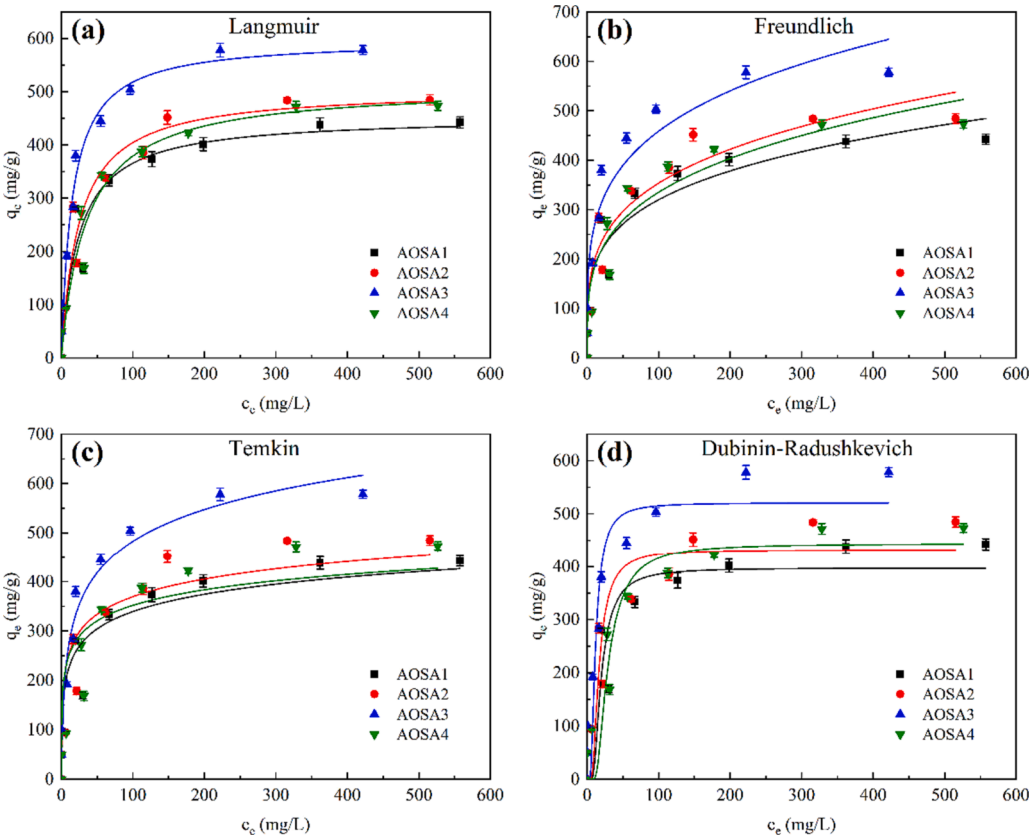

Fig. 9. Adsorption isotherm of Pb (II) on AOSA-X (conditions: V = 20 mL, pH = 5, T = 298 K, adsorbent dosage: 20 mg).

with increasing temperature. The positive ΔS^0 values illustrated that metal ions adsorption by AOSA-X became disordered at the solid–liquid interface. Thus, the adsorption was a spontaneous endothermic process.

3.2.6. *Selective adsorption of Pb (II) and Cu (II)*

It is essential to exploit the influence of selective adsorption processes of heavy metal ions considering the fact that only a single heavy metal ion exists rarely in real wastewater. The selective adsorption performance for Pb (II) and Cu (II) ions was elucidated by four common metal ions, such as Cd (II), Zn (II), Ni (II), and Mn (II) (Fig. S9). In a conical flask, 20 mL of each of the above four metal ions 0–50 mg/L with 20 mL of 50 mg/L of Pb (II) and Cu (II) ions were added respectively, and then 20 mg of AOSA3 adsorbent was added and adsorbed at pH 5.0 for 2 h for the selective adsorption experiments. The results indicated that the four interfering ions had a small influence on the adsorption of Pb (II) and Cu (II). When the concentrations of Cd (II), Zn (II), Ni (II), and Mn (II) were all 50 mg/L, the removal of Pb (II) decreased by 2.33%, 0.77%, 1.02% and 0.85%, respectively, and the removal of Cu (II) declined by 1.84%, 0.97%, 1.31% and 0.76%, respectively. The data revealed that AOSA3 has high selectivity and affinity for Pb (II) and Cu (II), demonstrating its potential to operate effectively in complicated heavy metal effluents.

3.2.7. *Recycling performance*

The recycling of the adsorbents is a key factor in assessing their performance for practical applications. In a 20 mL solution containing 50 mg/L heavy metal ions, 20 mg of AOSA3 was used for the adsorption, and then 25 mL of 0.1 M HCl was used as the eluent solution with an elution time of 180 min, causing the Pb (II) and Cu (II) ions anchored on AOSA3 to be released from the surface of the aerogel adsorbent into the elution solution. The adsorbent successfully underwent five consecutive adsorption–desorption cycles, the removal rate of AOSA3 for Pb (II) and Cu (II) dropped from 100% and 97.12% to 90.86% and 86.28%, and the adsorption capacity of AOSA3 for Pb (II) and Cu (II) dropped from 50 mg/g and 48.56 mg/g to 45.43 mg/g and 43.14 mg/g, respectively (Fig. 12). From the above data, it may be attributed to incomplete desorption during the acid-washing process, leading to some adsorption sites were not successfully eluted and some of the amidoxime groups were lost [64]. The regeneration experiments results indicated that the AOSA3 exhibited promising practical applications for the removal and recovery of metal ions from effluents.

3.3. *Adsorption mechanism*

The adsorption mechanism for metal ions adsorption by AOSA3 was revealed by XPS analysis. As illustrated in Fig. 13a, the total spectrum of AOSA3 displayed four elements, including C, Si, N and O. The AOSA3-Pb sample appeared at 138 eV with a new peak associated with Pb 4f after Pb (II) adsorption, with the peaks at 434 and 413 eV being associated with Pb 4d3/2 and Pb 4d5/2, respectively [65]. Similarly, the AOSA3-Cu sample exhibited the Cu 2p peak characterized at 934 eV following Cu (II) adsorption. The spectra of Pb 4f of AOSA3-Pb was presented in Fig. 13b, where the two peaks at 138.63 and 143.56 eV were assigned to Pb 4f7/2 and Pb 4f5/2, respectively [66]. Fig. 13c provided the Cu 2p spectrum of AOSA3-Cu, where the peaks at 934.96 and 954.63 eV belong to Cu 2p3/2 and Cu 2p1/2, and there was a satellite peak at 942.98 eV [49]. These results verified the successful adsorption of Pb (II) and Cu (II) ions by AOSA3.

Fig. 13d showed the N 1s spectrum of AOSA3, which was matched to two peaks, C–NH_2 (400.48 eV) and C=N–OH (399.14 eV), respectively [67]. It was noticed in AOSA3-Pb sample that these two N 1s peaks from AOSA3 were shifted to 400.86 and 399.47 eV, respectively (Fig. 13e). Similarly, after Cu (II) adsorption, two peaks were observed for AOSA3-Cu moved to 400.81 and 399.63 eV, respectively (Fig. 13f). The rise of N 1s binding energy can be ascribed to the sharing of electrons between the N atoms with metal ions, which decreased the electron cloud density

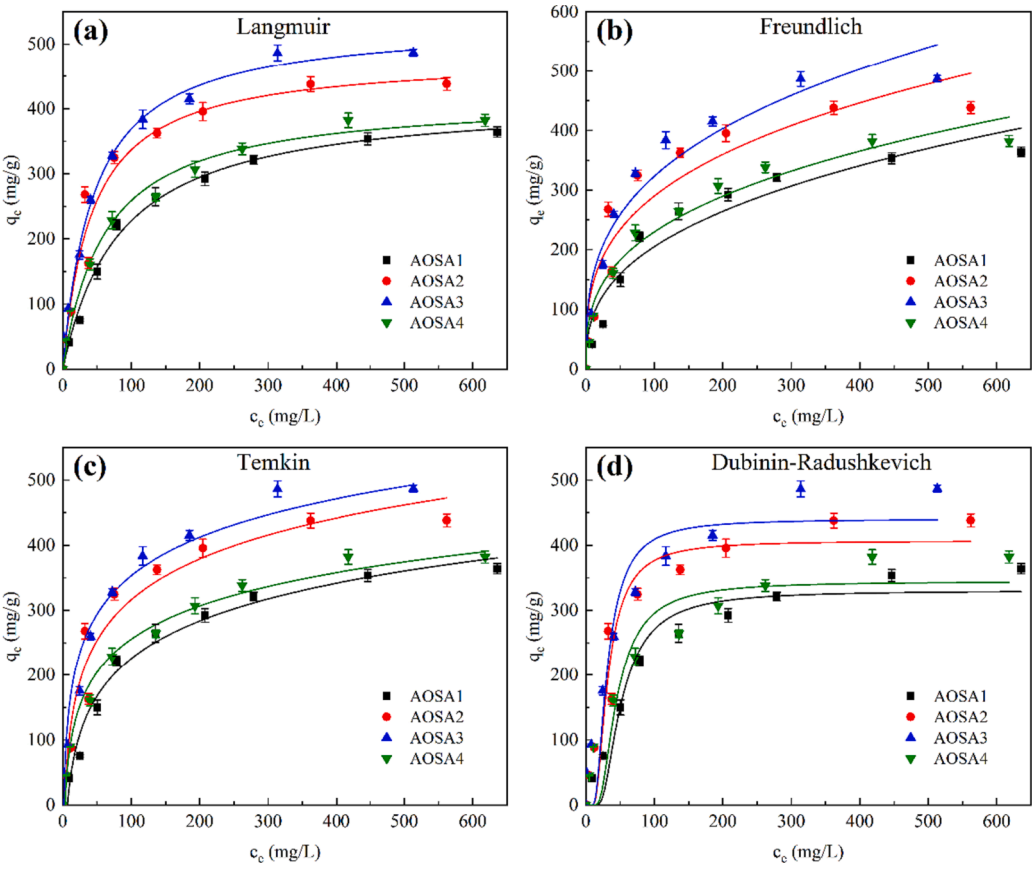

Fig. 10. Adsorption isotherm of Cu (II) on AOSA-X (conditions: V = 20 mL, pH = 5, T = 298 K, adsorbent dosage: 20 mg).

Table 3
Adsorption isotherm parameters for Pb (II) and Cu (II) onto AOSA-X.

Isotherms models	Parameters	Pb (II)				Cu (II)			
		AOSA1	AOSA2	AOSA3	AOSA4	AOSA1	AOSA2	AOSA3	AOSA4
Langmuir	k_L (L/mg)	0.0416	0.0401	0.0647	0.0285	0.0120	0.0233	0.0223	0.0162
	q_m (mg/g)	453.53	505.14	598.05	511.75	417.08	480.41	534.10	417.51
	R^2	0.9397	0.9527	0.9795	0.9619	0.9942	0.9666	0.9931	0.9884
Freundlich	k_F ((mg/g)/(mg/L)^n)	105.53	109.01	154.44	97.65	38.01	69.42	74.45	49.51
	n	0.2410	0.2555	0.2364	0.2678	0.3661	0.3105	0.3188	0.3335
	R^2	0.9288	0.9303	0.9412	0.9284	0.9418	0.9015	0.9570	0.9713
Temkin	k_T (L/g)	8.11	12.66	1.76	23.29	0.1473	0.3285	0.6258	0.3172
	B_T	50.64	51.71	93.29	45.39	83.82	90.53	85.35	73.88
	R^2	0.8883	0.8524	0.9715	0.8156	0.9835	0.9539	0.9645	0.9896
Dubinin-Radushkevich	k_{DR} (mol^2/kJ^2)	49.50	35.23	18.12	106.27	328.85	126.05	121.03	253.01
	q_{DR} (mg/g)	397.03	432.06	520.75	443.70	330.36	406.54	440.12	344.38
	E (kJ/mol)	0.1421	0.1685	0.2349	0.0970	0.0551	0.0890	0.0909	0.0628
	R^2	0.8472	0.8701	0.9201	0.9145	0.9426	0.9055	0.9245	0.8967

around the N atoms, demonstrating that the N atoms on the amidoxime groups were all involved in metal ions adsorption [44].

The O 1s spectrum of AOSA3 was displayed in Fig. 13g, where three peaks at 533.36, 532.58 and 531.51 eV can be divided into C=N–OH, Si–O and O–H, respectively [68]. In Fig. 13h and i, the O 1s peaks attributing to Si–O and O–H were almost unchanged. However, the O 1s peaks for C=N–OH of AOSA3-Pb and AOSA3-Cu were shifted to 533.61 and 533.99 eV, respectively. This indicated that the O atom on the amidoxime groups of AOSA3 was engaged in the adsorption process, and the decreased of its outer electron cloud density caused an increase in the binding energy [48]. In conclusion, XPS analysis unveiled that the N and O atoms of the amidoxime groups have participated in Pb (II) and Cu (II) adsorption process.

In addition, the ^{1}H NMR and ^{13}C NMR spectra of AO-Pb (II) and AO-Cu (II) were presented in Fig. S3, both amino and hydroxyl signal intensities decreased after the adsorption of Pb (II) and Cu (II) ions, suggesting that they have robust interactions with heavy metal ions. However, after interaction with Pb (II) and Cu (II) ions, there was almost no change in ^{13}C NMR spectrum, demonstrating that the metal ions did not interact with the backbone [69].

Table 4
Comparison of adsorption capacity of AOSA-X adsorbent with other amidoxime base adsorbents.

Adsorbents	Conditions	q_m (mg/g)		Reference
		Pb (II)	Cu (II)	
AO-PP fiber	T = 298 K, pH = 5	45.64	47.23	[28]
Amidoxime-functionalized mesoporous silica microsphere	T = 298 K, pH = 6.3	284	–	[30]
Fe_3O_4@SiO_2-g-PAMAM-AO magnetic composites	T = 318 K, pH = 5.5	157.25	–	[50]
PAN-Na-Y-zeolite composite	T = 298 K, pH = 4	74.2	48.5	[51]
PAO-AM chelating resin	T = 298 K, pH = 5.6, 5.4	331.5	185.6	[54]
CF-g-PAO cellulose	T = 298 K, pH = 5	25.16	25.65	[56]
Waste amidoxime chelating resin	T = 298 K, pH = 4	115.5	93.8	[60]
AM/AO/AEBI-CTS chitosan	T = 298 K, pH = 5	–	190.7	[61]
Amidoximated non-woven polyethylene-g-acrylonitrile fabric	T = 298 K, pH = 5.4, 5.2	107	74.62	[62]
AOSA1	T = 298 K, pH = 5	453.53	417.08	This work
AOSA2	T = 298 K, pH = 5	505.14	480.40	This work
AOSA3	T = 298 K, pH = 5	598.05	534.10	This work
AOSA4	T = 298 K, pH = 5	511.75	417.51	This work

The adsorption mechanism was further revealed by DFT calculations, explaining the possible role of distinct groups contributing to the adsorption. Fig. S10 illustrated the optimized structures of AOSA3, AOSA3-Pb and AOSA3-Cu. Adsorption energy (E_{ads}) smaller than 0 represents favorable adsorption and E_{ads} greater than 0 refers to adverse adsorption. DFT calculations showed that AOSA3-Pb had smaller E_{ads} (−0.71 eV) than AOSA3-Cu (−0.69 eV), suggesting that the adsorption of Pb (II) by AOSA3 had more stability than for Cu (II). HOMO and LUMO were used to describe the ability to donate and acquire electrons, respectively [70]. Fig. 14 showed the orbital diagrams of the HOMO-LUMO and E_{gap} changes for AOSA3, AOSA3-Pb and AOSA3-Cu. The HOMO and LUMO of AOSA3 was mainly located on the amidoxime groups. After metal ions adsorption by AOSA3, however, the HOMO and LUMO of both AOSA3-Pb and AOSA3-Cu changed significantly, indicating that AOSA3 successfully adsorbed Pb (II) and Cu (II). Moreover, the E_{gap} of AOSA3-Pb and AOSA3-Cu was remarkably reduced, suggesting that the original structure of AOSA3 was destroyed after metal ions adsorption [71].

Natural Bond Orbital (NBO) analysis further revealed the adsorption mechanism of the AOSA3 adsorbent interacting with Pb (II) and Cu (II) [72]. If the stability energy ($E^{(2)}$) is greater, the electron-donor and electron-acceptor interactions will be more powerful [73]. The adsorption of metal ions by AOSA3 was mainly dominated by the interaction of N and O atoms providing lone pairs electrons with Pb (II) and Cu (II). From Table S3, it can be observed that AOSA3-Pb exhibited $E^{(2)}$ values of 44.21 and 0.30 kcal/mol for LP(N10) → LP*(Pb) and LP(N12) → LP*(Pb), respectively, and $E^{(2)}$ value of 0.69 kcal/mol for LP(O11) → LP*(Pb). The $E^{(2)}$ value for LP(N10) → LP*(Pb) was larger than that for LP(O11) → LP*(Pb), illustrating that the N atom of the amidoxime group on AOSA3 had a predominant role in Pb (II) adsorption, and the N and O atoms were both participated in the adsorption process.

Similar results were observed in AOSA3-Cu, for which the $E^{(2)}$ values for LP(N10) → LP*(Cu) being larger than LP(O11) → LP*(Cu), suggesting the dominance of the N atom of the amidoxime functional groups for the Cu (II) adsorption [74]. In addition, the smaller $E^{(2)}$ value of LP(N) → LP*(Cu) than LP(N) → LP*(Pb), demonstrating that the binding affinity of AOSA3 for Pb (II) was superior to Cu (II) [75]. In conclusion, DFT calculations verified the key role of the amidoxime group in the adsorption of metal ions by AOSA3 and clearly elucidated the roles of various atoms contributing to the adsorption.

3.4. LCA analysis

3.4.1. Environmental impact of AOSA3 production

The environmental effects of preparing 1 kg of AOSA3 sample were assessed using the LCA method, as AOSA3 showed optimum adsorption performance (Section 3.2). As shown in Table S4, the mean values for PED, POFP, ODP, EP, ADP, AP and GWP were 1439.66 MJ, 0.21 kg NMVOC eq, 9.53E-06 kg CFC^{-11} eq, 0.04 kg PO_4^{3-} eq, 0.009 kg antimony eq, 0.29 kg SO_2 eq and 69.02 kg CO_2 eq. Among them, PED had the largest effect with 1439.66 MJ. The GWP value was not negligible because producing 1 kg of AOSA3 simultaneously produced 69.02 kg CO_2 eq. It is beneficial to find more eco-friendly AOSA3 production solutions by analyzing the impact of various feedstocks for AOSA3 production.

For a clearer analysis of the environmental effects of the AOSA3 adsorbent in the production process, the environment effect classification of all ingredients was standardized so that the sum of the factors for each effect classification was 100%. As presented in Fig. 15, ethanol had the highest percentage of environmental impacts among all ingredients

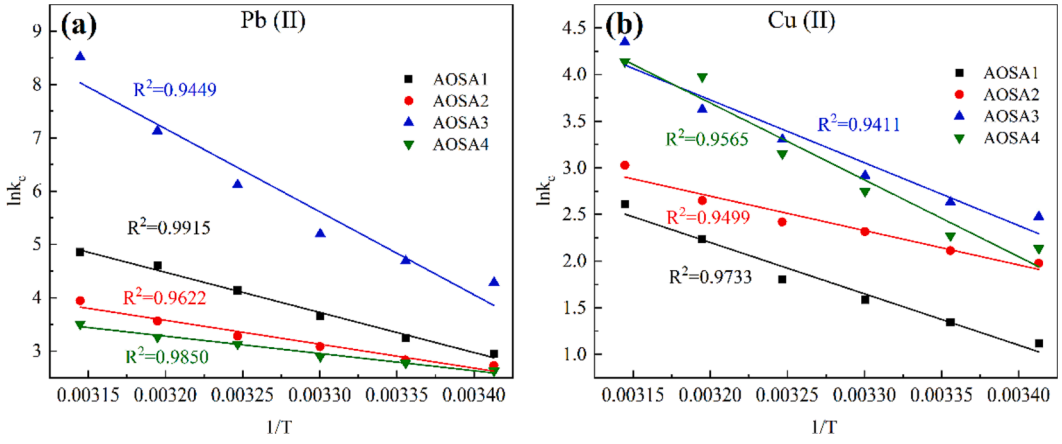

Fig. 11. The plots of lnk_c vs $1/T$ for the adsorption of Pb (II) (a) and Cu (II) (b) by AOSA-X (conditions: V = 20 mL, pH = 5, c_0 = 100 mg/L, adsorbent dosage: 20 mg).

Table 5
Thermodynamic parameters for Pb (II) and Cu (II) adsorption onto AOSA-X.

Samples	T/K	Pb (II)			Cu (II)		
		$\triangle G^0$/(kJ/mol)	$\triangle H^0$/(kJ/mol)	$\triangle S^0$/(J/(mol·K)	$\triangle G^0$/(kJ/mol)	$\triangle H^0$/(kJ/mol)	$\triangle S^0$/(J/(mol·K)
AOSA1	293	−7.00	62.58	237.48	−2.50	45.76	164.72
	298	−8.18			−3.32		
	303	−9.37			−4.15		
	308	−10.56			−4.97		
	313	−11.75			−5.79		
	318	−12.94			−6.62		
AOSA2	293	−6.38	37.27	149.01	−4.65	30.68	120.60
	298	−7.13			−5.26		
	303	−7.87			−5.86		
	308	−8.62			−6.46		
	313	−9.36			−7.06		
	318	−10.11			−7.67		
AOSA3	293	−9.39	129.45	473.88	−5.58	56.02	210.26
	298	−11.76			−6.64		
	303	−14.13			−7.68		
	308	−16.49			−8.74		
	313	−18.87			−9.79		
	318	−21.23			−10.84		
AOSA4	293	−6.31	26.95	113.50	−4.72	−68.56	250.11
	298	−6.87			−5.97		
	303	−7.44			−7.22		
	308	−8.01			−8.47		
	313	−8.57			−9.73		
	318	−9.14			−10.98		

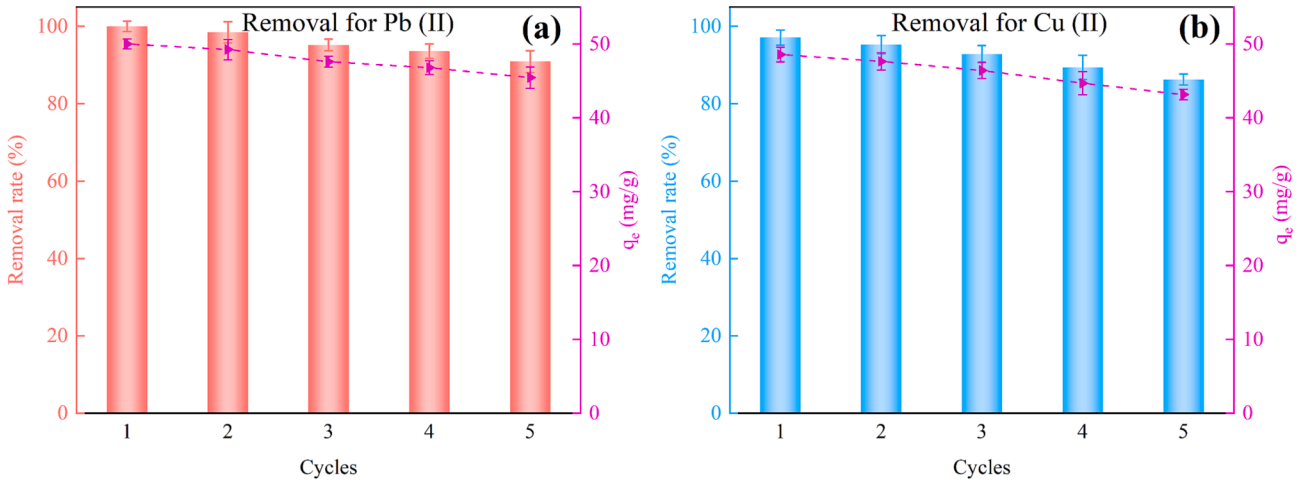

Fig. 12. Regeneration tests of AOSA3 (conditions: c_0 = 50 mg/L, pH = 5, T = 298 K, adsorbent dosage: 20 mg).

used in production. Its contribution to PED, POFP, ODP, EP, ADP, AP and GWP was 60.47%, 53.53%, 45.73%, 35.12%, 54.69%, 56.6% and 70.51%, respectively. This may be due to the role of ethanol primarily as a solvent and detergent in adsorbent preparation processes, where the higher quantity needed results in greater environmental effects. This was followed by n-Hexane, which contributed 25.19%, 38.48%, 46.9%, 37.25%, 38.23%, 17.05% and 8.89% to PED, POFP, ODP, EP, ADP, AP and GWP, respectively. The multiple usage of n-Hexane as a detergent made its environmental contribution proportionally higher. From Table 1, it was found that the TEOS dosage was only 0.62 kg, accounting for about 3.38% of the n-Hexane dosage, but caused a contribution of 23.88% to the EP in the synthesis stage of AOSA3. In addition, the consumption of electricity in the production of AOSA3 also accounted for a relatively large proportion of the GWP and AP, with 14.01% and 17.48%, respectively.

3.4.2. *Green production recommendations*

To provide a green and environmentally friendly method for sorbent synthesis, the environmental effects of the production process of AOSA3 have been analyzed. It is important to mitigate the negative impact on the environment by developing a technology to capture and reuse evaporated ethanol and n-Hexane, as they are easily volatilized. Considering the environmental impact of TEOS, it can be replaced by water glass, which can be used for preparation at a lower cost than the approach using TEOS, providing environmental and economic benefits in large-scale production [76]. The environmental impact of electricity can be replaced by tidal energy or wind power, which will protect the environment.

The environmental impact of the CTES synthesis process was also probed, due to the presence of the cyano group in CTES, which is a key feedstock for the introduction of the amidoxime group.

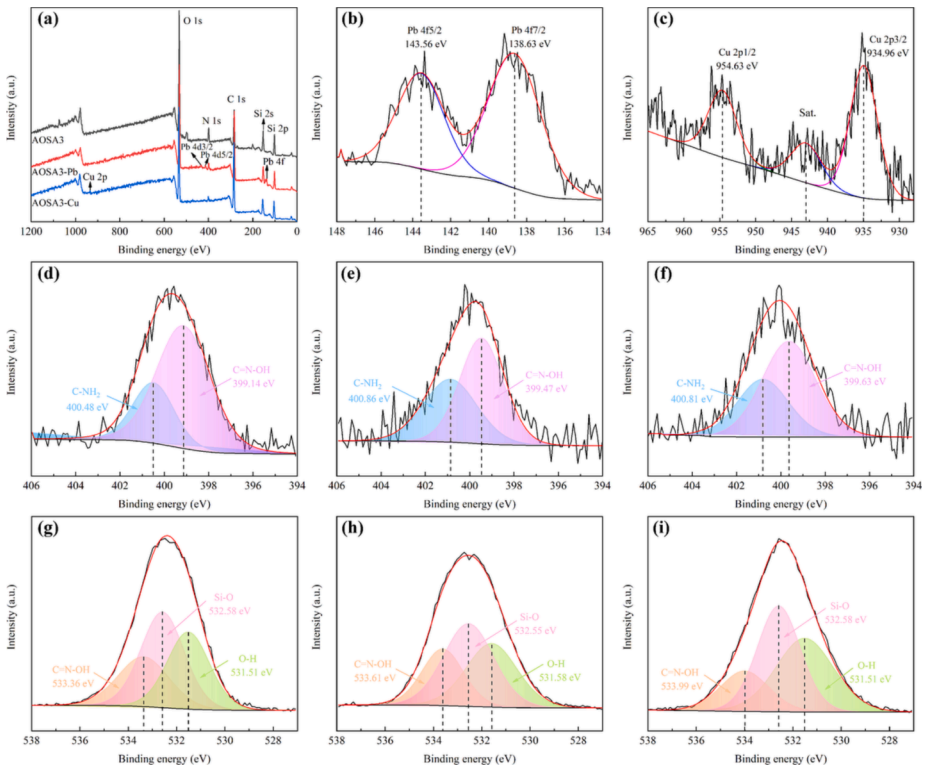

Fig. 13. XPS spectra of AOSA3: (a) full-scan spectra; (b) spectra of Pb 4f; (c) spectra of Cu 2p; N 1s spectra of AOSA3 (d), AOSA3-Pb (e) and AOSA3-Cu (f); O 1s spectra of AOSA3 (g), AOSA3-Pb (h) and AOSA3-Cu (i).

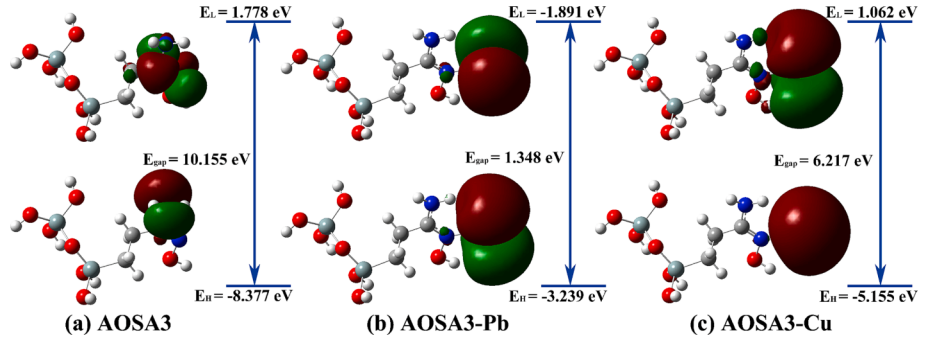

Fig. 14. Orbital diagram of the changes in HOMO-LUMO and E_{gap} for AOSA3 (a), AOSA3-Pb (b) and AOSA3-Cu (c).

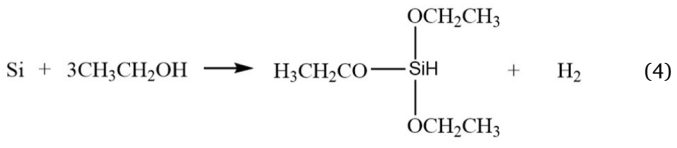

(4)

CTES was prepared from ethanol, silicon and acrylonitrile. To explain their impact on the environment, the above-mentioned factors were normalized to 100% in each impact category. In Fig. 16, among all ingredients, silicon had a particularly small environmental impact (close to 0%), while the environmental impacts of ethanol and acrylonitrile were more obvious. Ethanol contributed 51.67%, 66.67%, 53.33%, 30.77%, 52.73%, 41.67% and 52.85% to PED, POFP, ODP, EP, ADP, AP

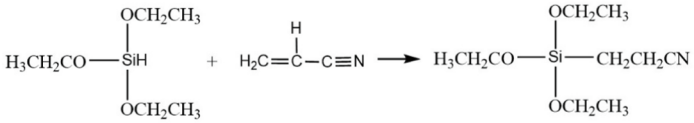

(5)

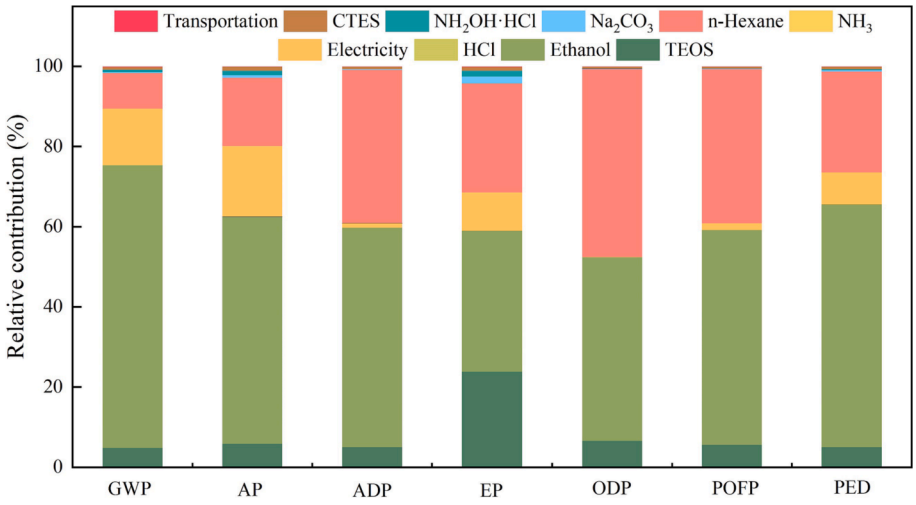

Fig. 15. The relative contribution of the AOSA3 preparation process to environmental indicators.

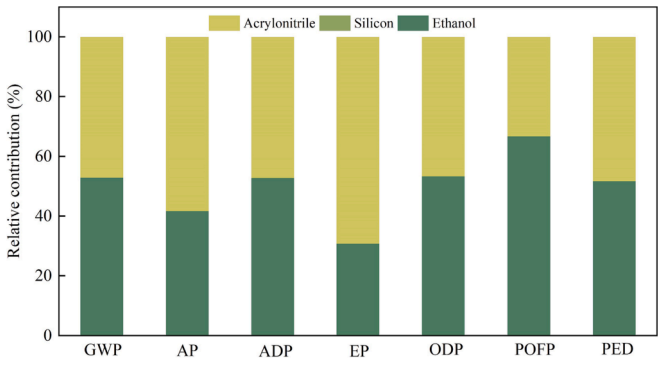

Fig. 16. The relative contribution of the CTES preparation process to environmental indicators.

and GWP, respectively. While acrylonitrile contributed 48.33%, 33.33%, 46.67%, 69.23%, 47.27%, 58.33% and 47.14% to the impacts of the above environmental categories, respectively. As described previously, the environmental effects of ethanol may be mitigated by recycling methods, finding other materials to replace acrylonitrile in the synthesis of CTES may also reduce the environmental impact.

4. Conclusion

Cyano-functionalized silica aerogel (ANSA-X) was obtained using ethyl orthosilicate as the silica source and 2-cyanoethyltriethoxysilane as the functionalization reagent, followed by reaction with hydroxylamine hydrochloride under alkaline condition to obtain amidoxime-functionalized silica aerogel (AOSA-X). SEM, FTIR, XRD, BET, ^{1}H and ^{13}C NMR, thermogravimetry, elemental analysis and XPS analysis were used for the characterization of the adsorbents with respect to their micro-morphology, structural composition and thermal stability. SEM results displayed the surface of the AOSA-X material had a porous structure. FTIR analysis indicated that the ANSA-X sample had a cyanogenic peak at 2260 cm^{-1}, and after the amidoxime modification, no cyano peak could be observed in the AOSA-X sample, which proved that the cyano group had been successfully reacted to produce the amidoxime group. BET analysis exhibited that AOSA2 had the largest specific surface area, followed by AOSA3. The adsorption isotherm experiments exhibited that the maximum adsorption capacity (q_m) of AOSA1, AOSA2, AOSA3, and AOSA4 for Pb (II) were 453.53, 505.14, 598.05, and 511.75 mg/g, and the maximum capacity (q_m) for Cu (II) were 417.08, 480.40, 534.10 and 417.51 mg/g, respectively. AOSA3 showed the optimum adsorption for metal ions. The adsorption kinetic studies revealed that AOSA-X could reach adsorption equilibrium in 120 min for Cu (II) and 60 min for Pb (II), and the adsorption was consistent with the pseudo-first-order and pseudo-second-order kinetic model. The adsorption thermodynamics demonstrated that adsorption was a spontaneous endothermic process, and the randomness at the solid–liquid interface increased. XPS analysis, NMR analysis and DFT theoretical calculations unveiled that the adsorption of metal ions by AOSA3 mainly occurred through the formation of coordination bonds with Pb (II) and Cu (II) by N and O atom donors on the amidoxime moiety, and the amidoxime moiety exhibited a strong metal ions coordination ability and a greater affinity for Pb (II). Several factors with high environmental impacts were obtained by LCA analysis, and the preparation strategy with clean production, energy saving and environmental protection was proposed.

CRediT authorship contribution statement

Yaoyao Zhang: Writing – original draft, Investigation, Conceptualization, Methodology, Validation, Data curation, Formal analysis. **Shikui Jia:** Methodology, Funding acquisition, Writing – review & editing. **Xinqiang Yuan:** Investigation, Writing – review & editing. **Liu Ding:** Validation, Writing – review & editing. **Taotao Ai:** Formal analysis, Writing – review & editing. **Kangze Yuan:** Writing – original draft, Writing – review & editing. **Wei Wang:** Methodology, Funding acquisition, Supervision, Writing – review & editing. **Luca Magagnin:** Supervision, Writing – review & editing. **Zhenyi Jiang:** Resources.

Declaration of Competing Interest

The authors declare that they have no known competing financial interests or personal relationships that could have appeared to influence the work reported in this paper.

Data availability

Data will be made available on request.

Acknowledgments

This work was supported by National Natural Science Foundation of China (52263004), the Innovative Research Team for Science and Technology of Shaanxi Province (2022TD-04), the National Foreign Expert Project of China (G2021171031L), and the Natural Science Foundation of Shaanxi University of Technology (grant No.

SLGRCQD2315, grant No. SLGKYXM2305).

Appendix A. Supplementary material

Supplementary data to this article can be found online at https://doi.org/10.1016/j.seppur.2023.126079.

References

[1] M.A.T.M.T. Rahman, M. Paul, N. Bhoumik, M. Hassan, M.K. Alam, Z. Aktar, Heavy metal pollution assessment in the groundwater of the Meghna Ghat industrial area, Bangladesh, by using water pollution indices approach, Appl. Water Sci. 10 (8) (2020) 186, https://doi.org/10.1007/s13201-020-01266-4.

[2] V.V. Dev, K.K. Nair, G. Baburaj, K.A. Krishnan, Pushing the boundaries of heavy metal adsorption: a commentary on strategies to improve adsorption efficiency and modulate process mechanisms, Colloid Interface Sci. Commun. 49 (2022), 100626, https://doi.org/10.1016/j.colcom.2022.100626.

[3] J. R., B. Gurunathan, S. K, S. Varjani, H.H. Ngo, E. Gnansounou, Advancements in heavy metals removal from effluents employing nano-adsorbents: way towards cleaner production, Environ. Res. 203 (2022), 111815, https://doi.org/10.1016/j.envres.2021.111815.

[4] S. Shahraki, H.S. Delarami, F. Khosravi, Synthesis and characterization of an adsorptive Schiff base-chitosan nanocomposite for removal of Pb(II) ion from aqueous media, Int. J. Biol. Macromol. 139 (2019) 577–586, https://doi.org/10.1016/j.ijbiomac.2019.07.223.

[5] S. Tighadouini, O. Roby, S. Radi, Z. Lakbaibi, R. Saddik, Y.N. Mabkhot, Z. M. Almarhoon, Y. Garcia, A highly efficient environmental-friendly adsorbent based on Schiff base for removal of Cu(II) from aqueous solutions: a combined experimental and theoretical study, Molecules 26 (17) (2021) 5164, https://doi.org/10.3390/molecules26175164.

[6] M.C. Benalia, L. Youcef, M.G. Bouaziz, S. Achour, H. Menasra, Removal of heavy metals from industrial wastewater by chemical precipitation: mechanisms and sludge characterization, Arab. J. Sci. Eng. 47 (5) (2021) 5587–5599, https://doi.org/10.1007/s13369-021-05525-7.

[7] A. Singh, D.B. Pal, A. Mohammad, A. Alhazmi, S. Haque, T. Yoon, N. Srivastava, V. K. Gupta, Biological remediation technologies for dyes and heavy metals in wastewater treatment: new insight, Bioresour. Technol. 343 (2022), 126154, https://doi.org/10.1016/j.biortech.2021.126154.

[8] R. Castro-Muñoz, B.E. Barragán-Huerta, V. Fíla, P.C. Denis, R. Ruby-Figueroa, Current role of membrane technology: from the treatment of agro-industrial by-products up to the valorization of valuable compounds, Waste Biomass Valor. 9 (4) (2017) 513–529, https://doi.org/10.1007/s12649-017-0003-1.

[9] J.P. Bezzina, L.R. Ruder, R. Dawson, M.D. Ogden, Ion exchange removal of Cu(II), Fe(II), Pb(II) and Zn(II) from acid extracted sewage sludge - resin screening in weak acid media, Water Res. 158 (2019) 257–267, https://doi.org/10.1016/j.watres.2019.04.042.

[10] A. Kuleyin, H.E. Uysal, Recovery of copper ions from industrial wastewater by electrodeposition, Int. J. Electrochem. Sci. 15 (2) (2020) 1474–1485. https://doi.org/10.20964/2020.02.39.

[11] C. Lei, J. Gao, W. Ren, Y. Xie, S.Y.H. Abdalkarim, S. Wang, Q. Ni, J. Yao, Fabrication of metal-organic frameworks@cellulose aerogels composite materials for removal of heavy metal ions in water, Carbohydr. Polym. 205 (2019) 35–41, https://doi.org/10.1016/j.carbpol.2018.10.029.

[12] O.A. Oyetade, A.A. Skelton, V.O. Nyamori, S.B. Jonnalagadda, B.S. Martincigh, Experimental and DFT studies on the selective adsorption of Pb2+ and Zn2+ from aqueous solution by nitrogen-functionalized multiwalled carbon nanotubes, Sep. Purif. Technol. 188 (2017) 174–187, https://doi.org/10.1016/j.seppur.2017.07.022.

[13] W. Boulaiche, B. Hamdi, M. Trari, Removal of heavy metals by chitin: equilibrium, kinetic and thermodynamic studies, Appl. Water Sci. 9 (2) (2019) 39, https://doi.org/10.1007/s13201-019-0926-8.

[14] R.O. Zaman Brohi, M.Y. Khuhawar, R.B. Mahar, Graphene oxide functionalized with a Schiff Base for the removal of Pb(II) ions from contaminated water: experimental and modeling approach, J. Chem. Technol. Biotechnol. 95 (6) (2020) 1694–1704. https://doi.org/10.1002/jctb.6362.

[15] C. Fu, X. Zhu, X. Dong, P. Zhao, Z. Wang, Study of adsorption property and mechanism of lead(II) and cadmium(II) onto sulfhydryl modified attapulgite, Arab. J. Chem. 14 (2) (2021), 102960, https://doi.org/10.1016/j.arabjc.2020.102960.

[16] Y. Zhang, X. Cao, J. Sun, G. Wu, J. Wang, D. Zhang, Synthesis of pyridyl Schiff base functionalized SBA-15 mesoporous silica for the removal of Cu(II) and Pb(II) from aqueous solution, J. Sol-Gel Sci. Technol. 94 (3) (2019) 658–670, https://doi.org/10.1007/s10971-019-05205-x.

[17] E. Rahmanifar, F. Shiri, S. Shahraki, P. Karimi, Experimental design for removal of lead ions from water samples using an engineered novel chitosan functionalized Schiff-base adsorbent, Chem. Eng. Commun. 210 (11) (2023) 2022–2034, https://doi.org/10.1080/00986445.2023.2174862.

[18] L. Tian, K. Fu, S. Chen, J. Yao, L. Bian, Comparison of microscopic adsorption characteristics of Zn(II), Pb(II), and Cu(II) on kaolinite, Sci. Rep. 12 (1) (2022) 15936, https://doi.org/10.1038/s41598-022-20238-z.

[19] H. Zhang, F. Xu, J. Xue, S. Chen, J. Wang, Y. Yang, Enhanced removal of heavy metal ions from aqueous solution using manganese dioxide-loaded biochar: behavior and mechanism, Sci. Rep. 10 (1) (2020) 6067, https://doi.org/10.1038/s41598-020-63000-z.

[20] P. Ding, W. Song, C. Wang, Z. Yu, Adsorption of Cu(II) and Pb(II) from aqueous solutions onto a metakaolin-based geopolymer, Desalin. Water Treat. 158 (2019) 164–173, https://doi.org/10.5004/dwt.2019.24190.

[21] G. Li, J. Zhang, J. Liu, C. Sun, Z. Yan, Adsorption characteristics of white pottery clay towards Pb(II), Cu(II), and Cd(II), Arab. J. Geosci. 13 (13) (2020) 519, https://doi.org/10.1007/s12517-020-05507-3.

[22] H.W. Kwon, J. Park, D.W. Ha, Y.H. Kim, Removal of cationic and anionic heavy metal ions from aqueous phase by a HGMS and magnetized zeolite, IEEE T. Appl. Supercon. 33 (5) (2023) 1–4, https://doi.org/10.1109/TASC.2023.3241826.

[23] Y. Zhang, K. Yuan, L. Magagnin, X. Wu, Z. Jiang, W. Wang, Schiff base functionalized silica aerogels for enhanced removal of Pb (II) and Cu (II): performances, DFT calculations and LCA analysis, Chem. Eng. J. 462 (2023), 142019, https://doi.org/10.1016/j.cej.2023.142019.

[24] J.W. Wei, J.H. Wang, S.S. Zhao, L.L. Geng, Synthesis and copper(II) affinity performance of amidoxime functionalized mesoporous silica, J. Inorg. Mater. 31 (5) (2016) 449–453. https://doi.org/10.15541/jim20150483.

[25] D. Shao, J. Li, X. Wang, Poly(amidoxime)-reduced graphene oxide composites as adsorbents for the enrichment of uranium from seawater, Sci. China Chem. 57 (11) (2014) 1449–1458, https://doi.org/10.1007/s11426-014-5195-7.

[26] B. Gao, Y. Gao, Y. Li, Preparation and chelation adsorption property of composite chelating material poly(amidoxime)/SiO2 towards heavy metal ions, Chem. Eng. J. 158 (3) (2010) 542–549, https://doi.org/10.1016/j.cej.2010.01.046.

[27] G. Zhou, J. Zeng, S. Tang, Z. Bai, J. Jiang, H. Zhang, Y. Wang, Preparation of reusable cross-linked amidoxime polyacrylonitrile microspheres and their efficient adsorption of Cu (II) and Pb (II), Polym. Bull. 80 (9) (2022) 9811–9831, https://doi.org/10.1007/s00289-022-04534-2.

[28] D. Zhao, Z. Wang, S. Lu, X. Shi, An amidoxime-functionalized polypropylene fiber: COMPETITIVE removal of Cu(II), Pb(II) and Zn(II) from wastewater and subsequent sequestration in cement mortar, J. Clean. Prod. 274 (2020), 123049, https://doi.org/10.1016/j.jclepro.2020.123049.

[29] S. Taimur, M.I. Hassan, T. Yasin, Removal of copper using novel amidoxime based chelating nanohybrid adsorbent, Eur. Polym. J. 95 (2017) 93–104, https://doi.org/10.1016/j.eurpolymj.2017.08.004.

[30] Y. Xie, J. Wang, M. Wang, X. Ge, Fabrication of fibrous amidoxime-functionalized mesoporous silica microsphere and its selectively adsorption property for Pb2+ in aqueous solution, J. Hazard. Mater. 297 (2015) 66–73, https://doi.org/10.1016/j.jhazmat.2015.04.069.

[31] L. Xu, Y. Liu, J. Wang, Y. Tang, Z. Zhang, Selective adsorption of Pb2+ and Cu2+ on amino-modified attapulgite: kinetic, thermal dynamic and DFT studies, J. Hazard. Mater. 404 (2021), 124140, https://doi.org/10.1016/j.jhazmat.2020.124140.

[32] B. Pillain, P. Loubet, F. Pestalozzi, J. Woidasky, A. Erriguible, C. Aymonier, G. Sonnemann, Positioning supercritical solvolysis among innovative recycling and current waste management scenarios for carbon fiber reinforced plastics thanks to comparative life cycle assessment, J. Supercrit. Fluids 154 (2019), 104607, https://doi.org/10.1016/j.supflu.2019.104607.

[33] R. Abejón, A. Bala, I. Vázquez-Rowe, R. Aldaco, P. Fullana-i-Palmer, When plastic packaging should be preferred: Life cycle analysis of packages for fruit and vegetable distribution in the Spanish peninsular market, Resour. Conserv. Recy. 155 (2020), 104666, https://doi.org/10.1016/j.resconrec.2019.104666.

[34] H. Ghasemi-Mobtaker, A. Kaab, S. Rafiee, Application of life cycle analysis to assess environmental sustainability of wheat cultivation in the west of Iran, Energy 193 (2020), 116768, https://doi.org/10.1016/j.energy.2019.116768.

[35] M. Frisch, G. Trucks, H.B. Schlegel, G.E. Scuseria, M.A. Robb, J.R. Cheeseman, G. Scalmani, V. Barone, B. Mennucci, G. Petersson, Gaussian 09, Revision d.01. Gaussian, Wallingford CT, (2009) 201.

[36] L. Sellaoui, D.I. Mendoza-Castillo, H.E. Reynel-Ávila, B.A. Ávila-Camacho, L. L. Díaz-Muñoz, H. Ghalla, A. Bonilla-Petriciolet, A.B. Lamine, Understanding the adsorption of Pb2+, Hg2+ and Zn2+ from aqueous solution on a lignocellulosic biomass char using advanced statistical physics models and density functional theory simulations, Chem. Eng. J. 365 (2019) 305–316, https://doi.org/10.1016/j.cej.2019.02.052.

[37] B. Wang, J. Xuan, X. Yang, Z. Bai, Synergistic DFT-guided design and microfluidic synthesis of high-performance ion-imprinted biosorbents for selective heavy metal removal, Colloids Surf. A Physicochem. Eng. Asp. 626 (2021), 127030, https://doi.org/10.1016/j.colsurfa.2021.127030.

[38] K. Chen, Q. Feng, Y. Feng, D. Ma, D. Wang, Z. Liu, W. Zhu, X. Li, F. Qin, J. Feng, Ultrafast removal of humic acid by amine-modified silica aerogel: Insights from experiments and density functional theory calculation, Chem. Eng. J. 435 (2022), 135171, https://doi.org/10.1016/j.cej.2022.135171.

[39] Iso, Environmental management-life cycle assessment: principles and framework, ISO, Geneva, 2006.

[40] P.C. Ferrão, Industrial Ecology-Principles and Tools, 2009.

[41] H. Ammar, A.F. Shaaban, T.A. Lasheen, E.S.A. Nouh, Preparation of new modified silica gel terminated with phenylphosphonic acid-amide moieties for adsorption of uranium(VI) from aqueous solutions, J. Radioanal. Nucl. Chem. 331 (9) (2022) 3657–3670, https://doi.org/10.1007/s10967-022-08452-5.

[42] Y. Wang, X. Hu, Y. Liu, Y. Li, T. Lan, C. Wang, Y. Liu, D. Yuan, X. Cao, H. He, L. Zhou, Z. Liu, J.W. Chew, Assembly of three-dimensional ultralight poly (amidoxime)/graphene oxide nanoribbons aerogel for efficient removal of uranium (VI) from water samples, Sci. Total Environ. 765 (2021), 142686, https://doi.org/10.1016/j.scitotenv.2020.142686.

[43] J. Xiao, Y. Jing, X. Wang, Y. Yao, Y. Jia, Preconcentration of uranium(VI) from aqueous solution by amidoxime-functionalized microspheres silica material: kinetics, isotherm and mechanism study, Chemistryselect 3 (43) (2018) 12346–12356, https://doi.org/10.1002/slct.201802472.

[44] H. Li, Y. Wang, M. Ye, X. Zhang, H. Zhang, G. Wang, Y. Zhang, Hierarchically porous poly(amidoxime)/bacterial cellulose composite aerogel for highly efficient scavenging of heavy metals, J. Colloid Interface Sci. 600 (2021) 752–763, https://doi.org/10.1016/j.jcis.2021.05.071.
[45] I.A. Khan, M. Inaam Ul Hassan, H. Hussain, S.M. Shah, T. Yasin, Fabrication and characterization of amidoxime-functionalized silica decorated with copper: a catalytic assembly for rapid reduction of dyes, Turk. J. Chem. 45 (2) (2021) 410-419. https://doi.org/10.3906/kim-2007-49.
[46] B. Satilmis, T. Isık, M.M. Demir, T. Uyar, Amidoxime functionalized Polymers of Intrinsic Microporosity (PIM-1) electrospun ultrafine fibers for rapid removal of uranyl ions from water, Appl. Surf. Sci. 467–468 (2019) 648–657, https://doi.org/10.1016/j.apsusc.2018.10.210.
[47] D. Wang, J. Song, J. Wen, Y. Yuan, Z. Liu, S. Lin, H. Wang, H. Wang, S. Zhao, X. Zhao, M. Fang, M. Lei, B. Li, N. Wang, X. Wang, H. Wu, Significantly enhanced uranium extraction from seawater with mass produced fully amidoximated nanofiber adsorbent, Adv. Energy Mater. 8 (33) (2018) 1802607, https://doi.org/10.1002/aenm.201802607.
[48] J. Bai, S. Li, X. Ma, H. Yan, S. Su, S. Wang, J. Wang, Novel preparation of amidoxime functionalized hyper-cross-linked polymeric adsorbent on the efficient adsorption of uranium in aqueous solution, Micropor. Mesopor. Mater. 331 (2022), 111647, https://doi.org/10.1016/j.micromeso.2021.111647.
[49] M.L. Rahman, C.J. Fui, M.S. Sarjadi, S.E. Arshad, B. Musta, M.H. Abdullah, S. M. Sarkar, E.J. O'Reilly, Poly(amidoxime) ligand derived from waste palm fiber for the removal of heavy metals from electroplating wastewater, Environ. Sci. Pollut. Res. 27 (27) (2020) 34541–34556, https://doi.org/10.1007/s11356-020-09462-0.
[50] Y. Dai, D. Liu, J. Zou, S. Wang, Y. Zhou, Facile preparation of amidoxime-functionalized Fe3O4@SiO2-g-PAMAM-AO magnetic composites for enhanced adsorption of Pb(II) and Ni(II) from aqueous solution, RSC Adv. 9 (2019) 9171, https://doi.org/10.1039/c9ra00128j.
[51] K.Z. Elwakeel, A.A. El-Bindary, E.Y. Kouta, E. Guibal, Functionalization of polyacrylonitrile/Na-Y-zeolite composite with amidoxime groups for the sorption of Cu(II), Cd(II) and Pb(II) metal ions, Chem. Eng. J. 332 (2018) 727–736, https://doi.org/10.1016/j.cej.2017.09.091.
[52] X. Chen, S. Cai, N. Zhang, J. Yang, T. Peng, F. Yang, Biosorption of U(VI) and mechanisms by live and dead cells of Sphingopyxis sp. YF1, Environ. Sci. Pollut. Res. 30 (2023) 109469–109480, https://doi.org/10.1007/s11356-023-29881-z.
[53] E. Asuquo, A. Martin, P. Nzerem, F. Siperstein, X. Fan, Adsorption of Cd(II) and Pb (II) ions from aqueous solutions using mesoporous activated carbon adsorbent: equilibrium, kinetics and characterisation studies, J. Environ. Chem. Eng. 5 (2017) 679–698, https://doi.org/10.1016/j.jece.2016.12.043.
[54] A.F. Shaaban, D.A. Fadel, A.A. Mahmoud, M.A. Elkomy, S.M. Elbahy, Synthesis of a new chelating resin bearing amidoxime group for adsorption of Cu(II), Ni(II) and Pb(II) by batch and fixed-bed column methods, J. Environ. Chem. Eng. 2 (2014) 632–641, https://doi.org/10.1016/j.jece.2013.11.001.
[55] T. Tatsumi, Y. Tahara, M. Matsumoto, Adsorption of metallic ions on amidoxime-chitosan/cellulose hydrogels, Separations 8 (11) (2021) 202, https://doi.org/10.3390/separations8110202.
[56] Y. Yue, Y. Liu, W. Zhang, J. Guo, Y. Gong, Y. Yu, Amidoxime functionalized low-cost cellulose-based adsorbent derived from waste cigarette filters for efficient heavy metal removal, J. Environ. Chem. Eng. 10 (3) (2022), 107846, https://doi.org/10.1016/j.jece.2022.107846.
[57] H. Chen, Y. Gao, A. El-Naggar, N.K. Niazi, C. Sun, S.M. Shaheen, D. Hou, X. Yang, Z. Tang, Z. Liu, H. Hou, W. Chen, J. Rinklebe, M. Pohořelý, H. Wang, Enhanced sorption of trivalent antimony by chitosan-loaded biochar in aqueous solutions: characterization, performance and mechanisms, J. Hazard. Mater. 425 (2022), 127971, https://doi.org/10.1016/j.jhazmat.2021.127971.
[58] S. Fan, X. Fan, S. Wang, B. Li, N. Zhou, H. Xu, Effect of chitosan modification on the properties of magnetic porous biochar and its adsorption performance towards tetracycline and Cu^{2}+, Sustain. Chem. Pharm. 33 (2023), 101057 https://doi.org/10.1016/j.scp.2023.101057.
[59] M. Ahmad, S.S. Lee, A.U. Rajapaksha, M. Vithanage, M. Zhang, J.S. Cho, S.E. Lee, Y. Sik Ok, Trichloroethylene adsorption by pine needle biochars produced at various pyrolysis temperatures, Bioresour. Technol. 143 (2013) 615–622, https://doi.org/10.1016/j.biortech.2013.06.033.
[60] C. Zheng, C. He, Y. Yang, T. Fujita, G. Wang, W. Yang, Characterization of waste amidoxime chelating resin and its reutilization performance in adsorption of Pb(II), Cu(II), Cd(II) and Zn(II) ions, Metals 12 (1) (2022) 149, https://doi.org/10.3390/met12010149.
[61] Y. He, S. Gou, L. Zhou, L. Tang, T. Liu, L. Liu, M. Duan, Amidoxime-functionalized polyacrylamide-modified chitosan containing imidazoline groups for effective removal of Cu2+ and Ni2+, Carbohydr. Polym. 252 (2021), 117160 https://doi.org/10.1016/j.carbpol.2020.117160.
[62] N. Rahman, M.S. Hossen, A.R. Miah, M.M. Marjub, N.C. Dafader, S. Shahnaz, M. F. Alam, Removal of Cu(II), Pb(II) and Cr(VI) ions from aqueous solution using amidoximated non-woven polyethylene-g-acrylonitrile fabric, J. Environ. Health Sci. Eng. 17 (1) (2019) 183–194, https://doi.org/10.1007/s40201-019-00339-0.
[63] S. Yadav, A. Asthana, A.K. Singh, R. Chakraborty, S.S. Vidya, M.A.B.H. Susan, S.A. C. Carabineiro, Adsorption of cationic dyes, drugs and metal from aqueous solutions using a polymer composite of magnetic/β-cyclodextrin/activated charcoal/Na alginate: isotherm, kinetics and regeneration studies, J. Hazard. Mater. 409 (2021), 124840, https://doi.org/10.1016/j.jhazmat.2020.124840.
[64] L. Chang, Y. Cao, W. Peng, Y. Miao, S. Su, G. Fan, Y. Huang, C. Li, X. Song, Highly efficient and selective recovery of Cu(II) from wastewater via ion flotation with amidoxime functionalized graphene oxide as nano collector, Sep. Purif. Technol. 279 (2021), 119674, https://doi.org/10.1016/j.seppur.2021.119674.
[65] H. Wang, Q. Gao, H. Li, G. Wang, B. Han, K. Xia, C. Zhou, Hydrous titania nanosheets constructed hierarchical hollow microspheres as a highly efficient dual-use decontaminant for elimination of heavy metal ions and organic pollutants, Chem. Eng. J. 381 (2020), 122638, https://doi.org/10.1016/j.cej.2019.122638.
[66] R. Huang, N. Shao, L. Hou, X. Zhu, Fabrication of an efficient surface ion-imprinted polymer based on sandwich-like graphene oxide composite materials for fast and selective removal of lead ions, Colloids Surf. A 566 (2019) 218–228, https://doi.org/10.1016/j.colsurfa.2019.01.011.
[67] X. Liu, S. Xie, G. Wang, X. Huang, Y. Duan, H. Liu, Fabrication of environmentally sensitive amidoxime hydrogel for extraction of uranium (VI) from an aqueous solution, Colloids Surf. A Physicochem. Eng. Asp. 611 (2021), 125813, https://doi.org/10.1016/j.colsurfa.2020.125813.
[68] G.J. Jiao, J. Ma, J. Zhang, Y. Li, K. Liu, R. Sun, Porous and biofouling-resistant amidoxime-based hybrid hydrogel with excellent interfacial compatibility for high-performance recovery of uranium from seawater, Sep. Purif. Technol. 287 (2022), 120571, https://doi.org/10.1016/j.seppur.2022.120571.
[69] C. Xie, Z. Yu, W. Tong, K. Shehzad, W. Xu, J. Wang, J. Liu, Insights into the fluorescence sensing mechanism of scandium-based metal-organic frameworks by solid-state NMR spectroscopy, ChemistrySelect 4 (2019) 5291–5299, https://doi.org/10.1002/slct.201900821.
[70] M. Rezaei-Sameti, P. Zarei, NBO, AIM, HOMO-LUMO and thermodynamic investigation of the nitrate ion adsorption on the surface of pristine, Al and Ga doped BNNTs: a DFT study, Adsorption 24 (8) (2018) 757–767, https://doi.org/10.1007/s10450-018-9977-7.
[71] J. Zhang, T. Li, X. Li, Y. Liu, N. Li, Y. Wang, X. Li, A key role of inner-cation-π interaction in adsorption of Pb(II) on carbon nanotubes: experimental and DFT studies, J. Hazard. Mater. 412 (2021), 125187, https://doi.org/10.1016/j.jhazmat.2021.125187.
[72] Y. Niu, S. Zhao, G. Chen, R. Qu, C. Zhou, L. Wang, S. Feng, Combined theoretical and experimental study on the adsorption mechanism of poly(4-vinylbenzyl 2-hydroxyethyl) sulfide, sulfoxide, and sulfone for Hg(II) and Pb(II), J. Mol. Liq. 219 (2016) 1065–1070, https://doi.org/10.1016/j.molliq.2016.04.043.
[73] F.A. Bulat, A. Toro-Labbé, T. Brinck, J.S. Murray, P. Politzer, Quantitative analysis of molecular surfaces: areas, volumes, electrostatic potentials and average local ionization energies, J. Mol. Model. 16 (11) (2010) 1679–1691, https://doi.org/10.1007/s00894-010-0692-x.
[74] X. Song, Y. Niu, P. Zhang, C. Zhang, Z. Zhang, Y. Zhu, R. Qu, Removal of Co(II) from fuel ethanol by silica-gel supported PAMAM dendrimers: combined experimental and theoretical study, Fuel 199 (2017) 91–101, https://doi.org/10.1016/j.fuel.2017.02.076.
[75] Y. Zhou, L. Luan, B. Tang, Y. Niu, R. Qu, Y. Liu, W. Xu, Fabrication of Schiff base decorated PAMAM dendrimer/magnetic Fe3O4 for selective removal of aqueous Hg(II), Chem. Eng. J. 398 (2020), 125651, https://doi.org/10.1016/j.cej.2020.125651.
[76] N.G. Kobylinska, V.G. Kessler, G.A. Seisenbaeva, O.A. Dudarko, In situ functionalized mesoporous silicas for sustainable remediation strategies in removal of inorganic pollutants from contaminated environmental water, ACS Omega 7 (27) (2022) 23576–23590, https://doi.org/10.1021/acsomega.2c02151.